Tectonophysics 779 (2020) 228377

Contents lists available at ScienceDirect

Tectonophysics

journal homepage: www.elsevier.com/locate/tecto

Frictional properties of actinolite-chlorite gouge at hydrothermal conditions

Ayumi S. Okamoto[a,b], André R. Niemeijer[b], Toru Takeshita[a], Berend A. Verberne[c,*], Christopher J. Spiers[b]

[a] Department of Natural History Sciences, Graduate School of Sciences, Hokkaido University, Sapporo 060-0810, Japan
[b] Department of Earth Sciences, Utrecht University, Budapestlaan 4, 3584, CD, Utrecht, the Netherlands
[c] Geological Survey of Japan, National Institute of Advanced Industrial Science and Technology, 1-1-1 Higashi, Tsukuba, Ibaraki 305-8567, Japan

ARTICLE INFO

Keywords:
Actinolite
Chlorite
Subduction
Friction
Megathrust
Earthquake

ABSTRACT

Exhumed subduction zones frequently show widespread actinolite-chlorite (Act-Chl) dominated compositions, suggesting that this may play an important role in controlling megathrust fault slip. We investigate the frictional behavior of simulated Act-Chl (85:15) gouge mixtures derived from natural mafic metamorphic rocks, under hydrothermal conditions using a ring shear deformation apparatus. Experiments were performed at effective normal stresses (σ_n^{eff}) of 50–200 MPa, pore fluid pressures (P_f) of 50–200 MPa, at temperatures (T) of 23–600 °C. In each experiment we applied a shear displacement (x) of ~10 mm at a constant sliding velocity (v) of 10 μm/s, followed by v-stepping in the range 0.3–100 μm/s, and slide-hold-slide (SHS) tests with hold times (t) ranging from 3 s to 3000 s. We quantified the rate- and state-dependent friction parameter (a-b), and investigated the effect of t on fault healing ($\Delta\mu_{pk}$). The results showed no effects of temperature on the coefficient of friction ($\mu \approx 0.6$–0.7), or on (a-b), with some experiments showing persistent, displacement-hardening or -weakening trends. Nonetheless, effects of v and of normal stress ($\sigma_n = \sigma_n^{eff} + P_f$) on ($a$-$b$) fall into three temperature regimes: (1) T = 23–100 °C, (2) T = 200–400 °C, and (3) T = 500–600 °C. In Regimes (1) and (3), (a-b) > 0 for all conditions tested, whereas in Regime (2), (a-b) ≤ 0, at $\sigma_n^{eff} = P_f = 50$ MPa and v = 0.3–3 μm/s. We discuss on the origin of persistent displacement-hardening or -weakening trends observed, and assess the implications of our data for subduction zone seismogenesis. Extrapolation of (a-b)-data using multiple linear regression suggests that high pore pressure ratios (>0.9) are needed to promote seismogenesis in faults cutting actinolite-chlorite compositions.

1. Introduction

Megathrust earthquakes nucleate at or near the interface between a subducting oceanic plate and an overriding continental plate, often causing severe direct damage and, in some cases, catastrophic tsunamis (e.g., Hyndman et al., 1997; Simons et al., 2011). Besides megathrust earthquakes, slow slip phenomena are now also recognized to occur along-strike major subduction zones (Dragert et al., 2001; Obara, 2002; Shelly et al., 2006; Brown et al., 2009; Peng and Gomberg, 2010). Slow earthquakes and megathrust earthquakes are believed to be linked (Obara and Kato, 2016; Uchida et al., 2016), however, the deformation mechanisms which play a role remain generally poorly understood. To improve our understanding of subduction zone seismogenesis, fault rock compositions present at hypocentral conditions need to be investigated experimentally under in-situ conditions where the natural deformation mechanisms can be activated.

Upper oceanic crust is dominantly composed of gabbro and basalts, covered by a layer of pelagic sediment close to the trench (Fig. 1A) (Christensen and Salisbury, 1975; Spudich and Orcutt, 1980), which for most oceanic convergent settings measures <1 km thick (Heuret et al., 2012). Data from hydrothermal friction experiments on (simulated) faults composed of these rock types (He et al., 2007; Zhang et al., 2017), and of ocean floor sediments (Ikari et al., 2013; Sawai et al., 2014, 2017; Kurzawski et al., 2018; Rabinowitz et al., 2018; Boulton et al., 2019), have yielded important clues on the frictional behavior of faults cutting 'fresh' oceanic crust. However, upon subduction, basaltic/gabbroic compositions and pelagic sediments become progressively metamorphosed (e.g., Bebout, 2007), producing assemblages with likely quite different mechanical properties. Moreover, field observations of exhumed subduction zones demonstrate that megathrust faults can occur as a tectonic mélange of (metamorphosed) slab-top sediments and (meta-)mafic rock (Fagereng and Sibson, 2010; Fagereng, 2011; Raymond, 2019), leaving the original oceanic plate stratigraphy completely disrupted.

* Corresponding author.
E-mail address: bartverberne16@hotmail.com (B.A. Verberne).

https://doi.org/10.1016/j.tecto.2020.228377
Received 10 August 2019; Received in revised form 16 February 2020; Accepted 17 February 2020
Available online 20 February 2020

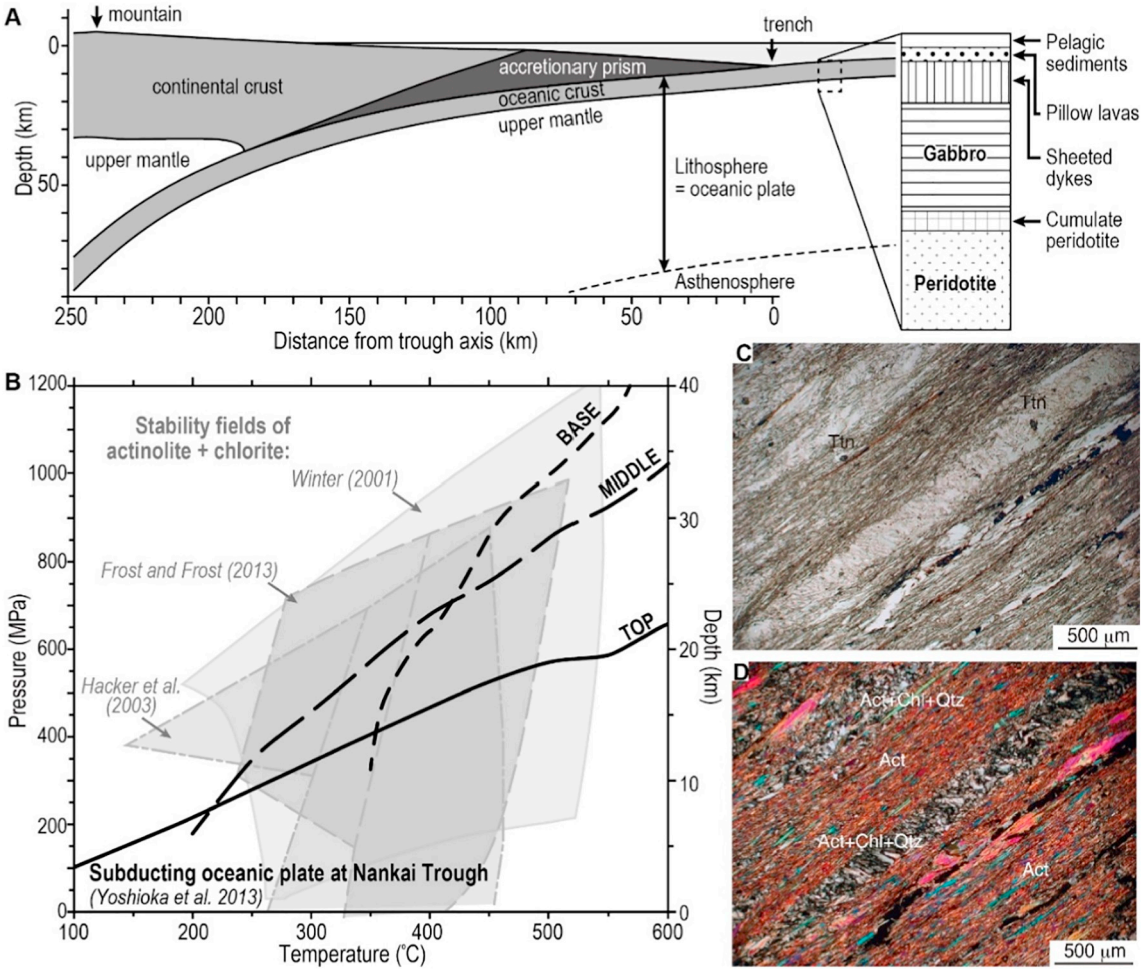

Fig. 1. (A) Schematic diagram of a subduction zone with an accretionary prism and a stratigraphic sequence of oceanic plate. (B) Actinolite + chlorite stability field and estimated pressure-temperature condition of the subducting oceanic Philippine plate at the Nankai Through, offshore Shikoku, Central Japan. The three stability fields are redrawn from the Prehnite-Pumpellyite and Greenschist facies of Winter (2001), Prehnite-Actinolite and Greenschist facies of Hacker et al. (2003), and Pumpellyite-Greenschist and Greenschist facies of Frost and Frost (2013). Black solid and dashed lines show the pressure-temperature conditions at depths corresponding to the top of the Philippine plate, and at 5 km (middle) and 10 km (base) from the top, as calculated for subduction under central Shikoku by Yoshioka et al. (2013) and assuming a density of 3.0 g/cm^3. (C) Plane polarized and (D) cross-polarized light micrographs of thin sections showing actinolite (Act) grains intercalated with lens-like layers composed of Act, chlorite (Chl), and quartz (Qtz). Ttn = titanite. Prepared from metasomatized serpentinites of the Sambagawa belt (Shikoku, Central Japan). See Fig. 3 of Takeshita et al. (2015) for the detailed sampling locality.

Realistic fault rock compositions which are believed to be present in a subduction zone, and which have been tested under in-situ hydrothermal conditions, include metapelite-like mixtures of illite + quartz (150–500 °C; Den Hartog et al., 2012a) and muscovite + quartz (100–600 °C; Den Hartog et al., 2013), serpentine (25–700 °C; Hirauchi et al., 2010; Chernak and Hirth, 2011; Takahashi et al., 2011; Moore and Lockner, 2013), lawsonite/blueschist (Okazaki and Hirth, 2016; Sawai et al., 2016), and chlorite (Okamoto et al., 2019). In addition to these compositions, field studies of exhumed subduction zones frequently point to the widespread occurrence of actinolite-chlorite assemblages (Nishiyama, 1989; Bebout and Barton, 2002; Sorensen et al., 2010; Takeshita et al., 2015), suggesting that this may play an important role in controlling deformation. Specifically, actinolite-dominated rocks are observed at the boundary between serpentinite and high-pressure/high-temperature metabasites and -sediments, representing a metasomatic reaction zone in the upper parts of the subducting oceanic plate. Examples include the Sambagawa belt (Shikoku, Central Japan, see Fig. 1C, D) (Takeshita et al., 2015), and the Nishisonogi metamorphic complex (Kyushu, Southern Japan), where actinolite-chlorite schists are believed to have acted as lubricants for tectonic transposition (Nishiyama, 1989).

The potentially important role of actinolite-chlorite assemblages in controlling megathrust fault deformation is also evident from a comparison of pressure-temperature (P-T) stability data (Winter, 2001; Hacker et al., 2003; Frost and Frost, 2013) with the projected P-T conditions of a subducting oceanic plate (Fig. 1B). In Fig. 1B, the projected P-T conditions of the Philippine plate (Yoshioka et al., 2013), which is subducting at the Nankai Trough offshore Shikoku (Japan), are drawn as black solid and dashed lines, with the stability fields of actinolite + chlorite in the background. The thickness of oceanic crust is typically less than ~7 km (e.g., Spudich and Orcutt, 1980), so that the long-dashed line for depths of 5 km is probably best representative for the P-T conditions of the intra-oceanic crust. In view of their stability over a wide range of conditions encompassing the subduction seismogenic zone, and their abundance in field exposures of subduction-metamorphosed rocks, fault rocks composed of actinolite-chlorite are accordingly expected to play an important role in controlling megathrust fault rheology.

Aiming to elucidate the mechanical properties of actinolite-chlorite fault rocks, we conducted hydrothermal friction experiments using mixtures of powdered actinolite (Act, ~85 wt%) + chlorite (Chl, ~15 wt%). We designed this composition to simulate a fine-grained metamorphic mineral paragenesis found to preferentially accommodate deformation in greenschist (GS) and prehnite-pumpellyite (sub-GS)

facies rocks, observed in field exposures of exhumed subduction zones in Japan. The ratio of Act/Chl which we selected for the experimental materials is arbitrary, simply based on the dominance of actinolite accompanied by lesser amount of chlorite in such natural fault rocks. All experiments were performed at normal stresses corresponding to pressures at ~3–13 km depth (i.e., effective normal stresses (σ_n^{eff}) of 50 MPa and pore fluid pressures (P_f) of 50–200 MPa), at temperatures of ~23–600 °C. We investigate how experimental variables, especially pore pressure ratio ($\lambda = P_f/\sigma_n$), affect the evolution of the friction coefficient (μ), the frictional velocity-dependence expressed using the rate- and state-dependent friction parameter (a-b), and fault healing ($\Delta\mu_{pk}$). We go on to extrapolate our findings to greater normal stresses and/or depths in a subduction zone, and we discuss the implications for subduction zone seismogenesis.

2. Materials and methods

2.1. Rock sampling and preparation for experiments

We collected samples of sheared and metamorphosed mafic rocks from the high-pressure/high-temperature Kamuikotan rocks (Hokkaido, North Japan), which were formed in a subduction zone in the Cretaceous (Sakakibara and Ota, 1994). Sectioned samples were analyzed using light and scanning electron microscopy (SEM), and compositional analyses was performed using an energy dispersive X-ray detector installed on the SEM. Amphibolites show a fine-grained (<100 μm) actinolite-chlorite matrix, with the long-axes of actinolite grains preferentially aligned in a foliation that is folded and locally cut by micro-fractures (Fig. 2A–D). However, the overall matrix texture appears ductilely deformed. The angular actinolite grains form a dense (low porosity) matrix with chlorite. Other major minerals, such as epidote, are suspended in the actinolite-chlorite matrix and show little internal deformation structures (Fig. 2A–C). These observations strongly suggest that only the fine-grained, actinolite-chlorite matrix has been deformed to large strains.

To simulate a fault gouge, we used a mixture of actinolite (amphibole) and clinochlore (chlorite), separated from an actinolite-dominated amphibolite collected from Higashi-Horai, Mitsuishi, Hokkaido, North Japan (42°15′31.7″N, 142°35′22.8″E). This amphibolite constitutes part of the boundary between serpentinite and metabasite in the Kamuikotan metamorphic rocks described above. To prepare the starting material, the rock was crushed, and then washed sequentially using tap water, 3 N hydrochloric acid, and pure water. The powder was then dried in an oven at ~40 °C for 24 h, and sieved to obtain a fraction with a grain size ranging between 50 and 150 μm. X-ray diffraction (XRD) analysis showed that the starting powder consisted of 85.12 wt% actinolite and 14.88 wt% clinochlore (85:15 mixture). Each experiment used ~0.6 g of sample powder and a starting layer thickness of ~1.5 mm.

2.2. Deformation apparatus

Frictional sliding experiments were performed using the hydrothermal ring shear apparatus installed at Utrecht University (as used by Okamoto et al., 2019). The apparatus consists of an internally heated, 300 MPa pressure vessel mounted in an Instron loading frame with

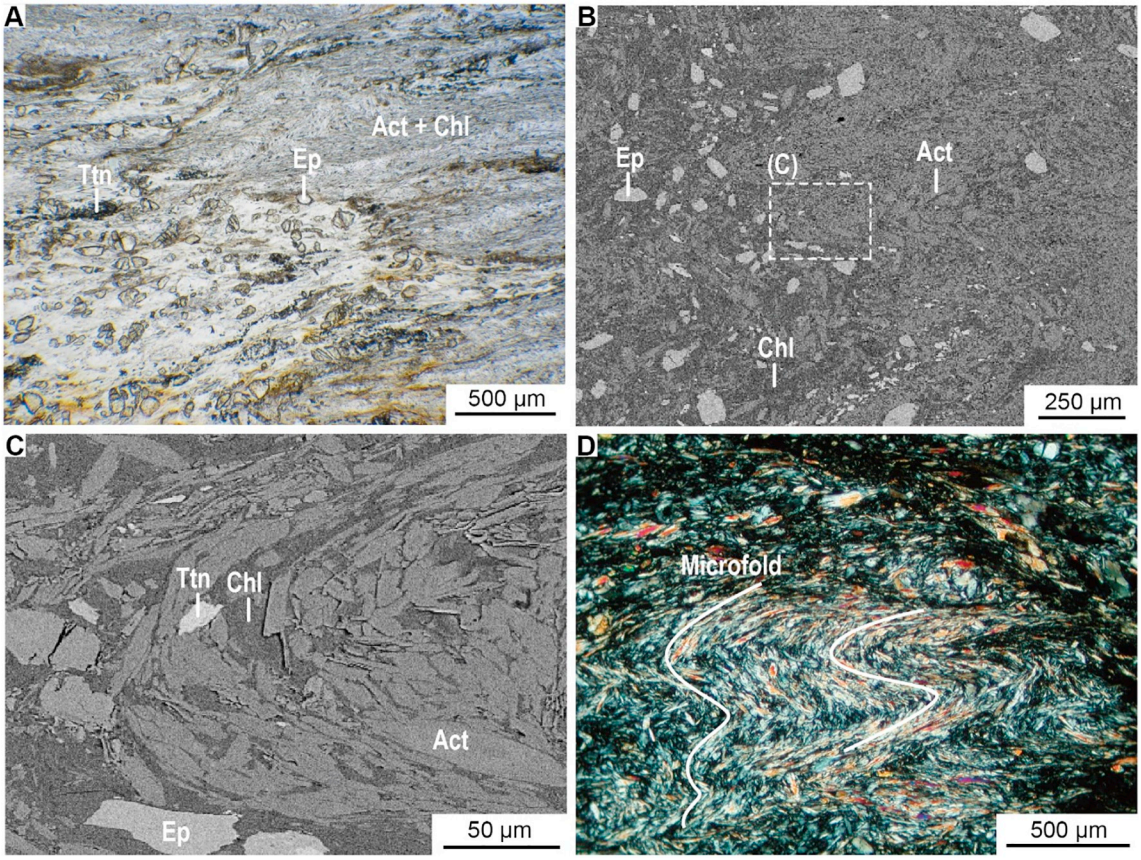

Fig. 2. Micrographs of thin sections prepared from rocks collected from an actinolite-dominated amphibolite from the Horokanai unit near the Horokanai Pass, Hokkaido, North Japan. (A) Actinolite (Act) and chlorite (Chl) grains surrounding epidote (Ep) and titanite (Ttn) (plane-polarized light). (B) Back-scattered electron (BSE) image of a part of the area shown in (A). (C) BSE image highlighting the dashed box shown in (B). Note that Act grains are fractured and gaps between them are filled with Chl. (D) Microfolds formed by an arrangement of elongate Act grains, in blueschist rocks with greenschist facies metamorphic overprint (crossed polarized light).

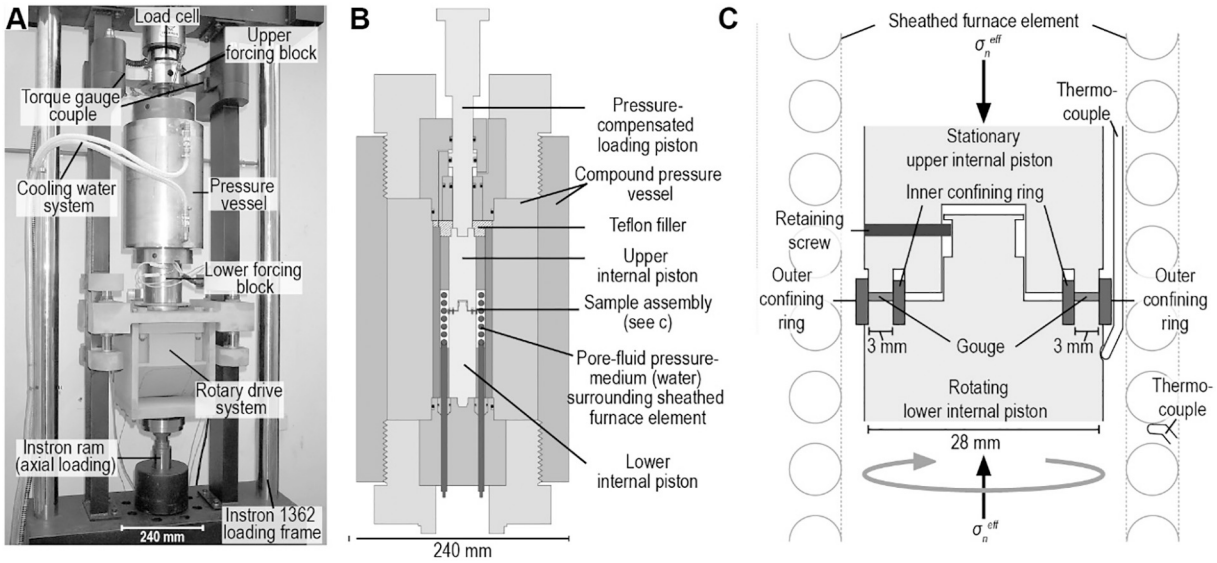

Fig. 3. Hydrothermal ring shear apparatus used in this study (after Den Hartog et al., 2012b). (A) Rotary shear drive system and pressure vessel mounted inside the Instron loading frame used to apply normal stress to the sample. (B) Semi-schematic cross section of the pressure vessel. External water-cooling jackets are not shown. (C) Semi-schematic cross section of the sample assembly. σ_n^{eff} = effective normal stress.

electrically actuated ram for axial loading, plus a rotation drive for imposing shear displacement onto the sample (Fig. 3A, B). The sample is sandwiched between René-41 Superalloy pistons, and prevented from being extruded using inner and outer confining rings that are coated using a graphite powder suspension to reduce wall friction (Fig. 3B, C). Repeat experiments performed later (u815, u822, u823) were carried out using a MoS_2-spray coating. The vessel is filled with distilled water, which acts as a pore fluid since the inner and outer confining rings are unsealed. Normal stress is applied to the sample in excess of the pore fluid pressure (P_f) measured in the vessel via a pressure-compensated upper loading piston, so that the effective normal stress (σ_n^{eff}) is equal to the axially applied stress (and normal stress $\sigma_n = \sigma_n^{eff} + P_f$). The applied normal force is measured externally and controlled using a 100 kN servo-controlled Instron loading frame. Temperature (T) is measured using two thermocouples, located on the furnace element near the sample and just below the sample (Fig. 3C). Rotation of the pressure vessel and lower internal piston allows shearing of the sample at constant rate. The shear stress (τ) is measured externally using a torque gauge couple (better than ±6 Nm) attached to the non-rotating upper piston, which is locked in an upper forcing block. Shear displacement is measured using a potentiometer attached to the rotating pressure vessel, and axial displacement is measured using two linear variable differential transformers (LVDTs), one integral to the Instron frame (with ±50 mm range) and a second one positioned to measure vessel displacement relative to the upper loading piston (with ±0.5 mm range).

2.3. Experimental conditions and procedure

We conducted 38 experiments in total, which we subdivided into Groups I–IV based on the effective normal stress (σ_n^{eff}) – pore fluid pressure (P_f) – temperature (T) conditions applied (see Table 1). Thirteen experiments were carried out under the same σ_n^{eff}-P_f-T conditions as in a previous run (i.e., representing repeat experiments) to check data reproducibility. Experiments from Groups I, II, and III used a pore fluid pressure ratio ($\lambda = P_f/\sigma_n$) of 0.5, T in the range from 23 °C to 600 °C, and σ_n^{eff}- and P_f-values of respectively 50 MPa, 100 MPa, and 200 MPa (or $\sigma_n = \sigma_n^{eff} + P_f$ = 100 MPa, 200 MPa, and 400 MPa). Due to the difficulty of controlling temperature above the critical point of water we were unable to conduct experiments in Group I using $T \geq 500$ °C. Experiments from Group IV are used T = 300 °C, and λ-values between 0.2 and 0.8 (by varying σ_n^{eff} and P_f —see Table 1).

In each experiment, before switching on the rotation drive hence imposing a shear displacement on the sample, the system was held at the desired σ_n^{eff}–P_f–T conditions for 1.5 to 2 h until all signals stabilized. We assume that this is sufficient time to establish chemical equilibrium between the pore fluid starting composition (distilled water) and the sample. The experimental approach employed for each test is summarized in Fig. 4. Each sample was initially sheared for a displacement (x) of ~10 mm using a constant motor drive velocity (v) of 10 μm/s. This was followed by a v-stepping test (Fig. 4), using stepwise changes of v in the sequence 0.3|1|3|10|30|100 μm/s in corresponding displacement intervals (Δx) of ~0.45|0.6|0.6|0.9|0.9|1.2 mm. We continued with 'slide-hold-slide' (SHS) tests (Fig. 4). Here, the sample was first sheared at v = 10 μm/s for $\Delta x \approx$ 2.5 mm, followed by switching-off of the rotation drive and maintaining constant piston position for a certain 'hold' time interval t_{hold}. We used sequentially increasing hold times of 3|10|30|100|300|1000|3000 s, with 'slide' intervals of $\Delta x \approx$ 1 mm at v = 10 μm/s. The cumulative shear displacement (x_{fnl}) in each experiment measured ~22.8–24.8 mm (Table 1), except in experiment Act12, during which a problem occurred upon sliding at the initial v = 10 μm/s (such that x_{fnl} = 39.6 mm). The layer thickness of the samples after the experiments measured 0.25–0.91 mm. Recovery of the sheared samples was extremely difficult due to disintegration after an experiment. We successfully recovered intact fragments from only a few experiments, implying that systematic post-mortem microstructural analysis was impossible. Recovered fragments were impregnated with an epoxy resin, and sectioned in an orientation normal to the shear plane and (sub-)parallel to the shear direction. Thin sections were analyzed using a Leica polarizing light microscope, and using a scanning electron microscope operated in backscattered electron (BSE) mode.

2.4. Data acquisition and processing

Shear displacement (digital resolution ±0.4 μm), axial displacement (±0.005 mm and ±0.05 μm during shearing), normal force (±0.05 kN), and torque (better than ±6 Nm) were measured externally and the corresponding signals logged, together with the pore fluid pressure (±0.005 MPa) and temperature (±1 °C) signals, using a 16 bit A/D converter and a logging frequency of 1–100 Hz. We characterize sample strength during shearing using the apparent coefficient of

Table 1
List of experiments, conditions, and key data.

Experiment	T (°C)	σ_n^{eff} (MPa)	P_f (MPa)	x_{fnl} (mm)	l_{fnl} (mm)	τ_{yld} (MPa)	μ_{yld}	τ_p (MPa)	μ_p	τ_x (MPa)	μ_x
Group I: $\sigma_n^{eff} = P_f = 50$ MPa ($\lambda = 0.5$)											
Act19	23	50	50	24.23	0.91	22.19	0.46	33.76	0.70	32.35	0.67
Act15	100	50	50	24.24	0.58	24.94	0.52	31.83	0.66	32.57	0.68
Act27	100	50	50	24.24	0.83	20.78	0.43	30.32	0.63	27.27	0.57
u815	100	50	50	24.84	n/a	24.60	0.50	31.97	0.65	32.91	0.67
Act16	200	50	50	24.15	0.66	24.57	0.51	31.84	0.66	28.69	0.60
Act25	200	50	50	24.26	0.65	23.76	0.49	30.62	0.64	30.01	0.62
Act17	300	50	50	24.21	0.87	21.85	0.45	32.80	0.68	28.93	0.60
Act18	400	50	50	24.29	0.90	21.35	0.44	30.39	0.63	30.28	0.63
Group II: $\sigma_n^{eff} = P_f = 100$ MPa ($\lambda = 0.5$)											
Act06	23	100	100	24.17	0.79	57.38	0.59	75.85	0.77	75.25	0.77
Act22	23	100	100	24.24	0.87	49.93	0.51	70.04	0.71	67.46	0.69
Act05	100	100	100	24.36	0.78	51.66	0.53	75.27	0.77	72.18	0.74
Act26	100	100	100	24.23	0.81	48.21	0.49	67.22	0.69	58.51	0.60
u821	100	100	100	24.57	n/a	47.51	0.49	63.34	0.65	57.32	0.59
Act03	200	100	100	24.33	0.25	58.79	0.60	70.31	0.72	72.81	0.74
Act04	300	100	100	24.47	0.27	56.27	0.57	63.52	0.65	72.24	0.74
Act01	400	100	100	24.25	0.91	53.26	0.54	64.49	0.66	59.50	0.61
Act20	400	100	100	24.16	0.82	48.40	0.50	70.21	0.72	59.19	0.60
Act07	500	100	100	24.29	0.61	46.20	0.47	75.63	0.77	66.73	0.68
Act02	600	100	100	24.34	0.51	49.90	0.51	70.31	0.72	75.54	0.77
Group III: $\sigma_n^{eff} = P_f = 200$ MPa ($\lambda = 0.5$)											
Act11	23	200	200	24.21	0.76	101.35	0.51	137.64	0.70	122.63	0.62
Act13	100	200	200	24.26	0.74	96.90	0.49	132.98	0.67	93.51	0.47
Act21	100	200	200	24.10	0.73	93.38	0.47	121.93	0.62	116.01	0.59
Act29	100	200	200	24.01	0.52	100.43	0.51	134.00	0.68	127.92	0.65
Act09	200	200	200	24.15	0.4	110.97	0.56	140.32	0.71	134.28	0.68
Act14	300	200	200	24.15	0.68	110.51	0.56	137.58	0.70	139.76	0.71
Act24	300	200	200	24.13	0.72	94.61	0.48	123.12	0.62	101.56	0.51
u822	300	200	200	22.84	n/a	111.277	0.57	147.42	0.75	150.67\	0.77
Act08	400	200	200	24.13	0.54	111.28	0.56	140.38	0.71	116.62	0.59
Act12	500	200	200	39.64	0.44	93.52	0.47	139.83	0.71	118.4	0.60
Act28	500	200	200	24.27	0.60	88.24	0.45	123.99	0.63	102.48	0.52
Act10	600	200	200	24.28	0.51	87.96	0.44	126.60	0.64	101.01	0.51
Act23	600	200	200	24.25	0.85	87.61	0.44	121.04	0.61	99.13	0.50
Group IV: Constant $T = 300$ °C ($\lambda = 0.2$ to 0.8)											
Act32	300	50	100	24.61	0.67	23.16	0.48	29.95	0.62	28.90	0.60
Act34	300	50	200	24.49	0.40	23.14	0.48	32.12	0.67	32.84	0.68
Act30	300	100	50	24.74	0.89	52.48	0.54	71.08	0.73	65.80	0.67
Act31	300	100	200	24.66	0.76	55.71	0.57	75.83	0.77	75.15	0.77
Act35	300	200	50	24.23	0.42	115.61	0.58	154.56	0.78	159.50	0.81
Act33	300	200	100	24.59	0.55	90.95	0.46	128.57	0.65	111.74	0.56

T = temperature; σ_n^{eff} = effective normal stress; P_f = pore fluid pressure; $\lambda = P_f/\sigma_n = P_f/(\sigma_n^{eff} + P_f)$ = pore fluid pressure ratio; x_{fnl} = total shear displacement; l_{fnl} = final layer thickness; τ_{yld} = shear stress at apparent yield; $\mu_{yld} = \tau_{yld}/\sigma_n^{eff}$; τ_p = peak shear stress at $x \leq 5$ mm; $\mu_p = \tau_p/\sigma_n^{eff}$; τ_x = shear stress at $x = 9.5$ mm; $\mu_x = \tau_x/\sigma_n^{eff}$.

friction, which was calculated as the shear stress divided by the effective normal stress ($\mu = \tau/\sigma_n^{eff}$), ignoring any cohesion. To obtain the effective normal stress (σ_n^{eff}) and shear stress (τ) acting on the sample, we corrected measured normal force and torque for seal friction using calibration tests carried out at the relevant conditions of pressure and temperature. The values of (effective) normal stress listed in Table 1

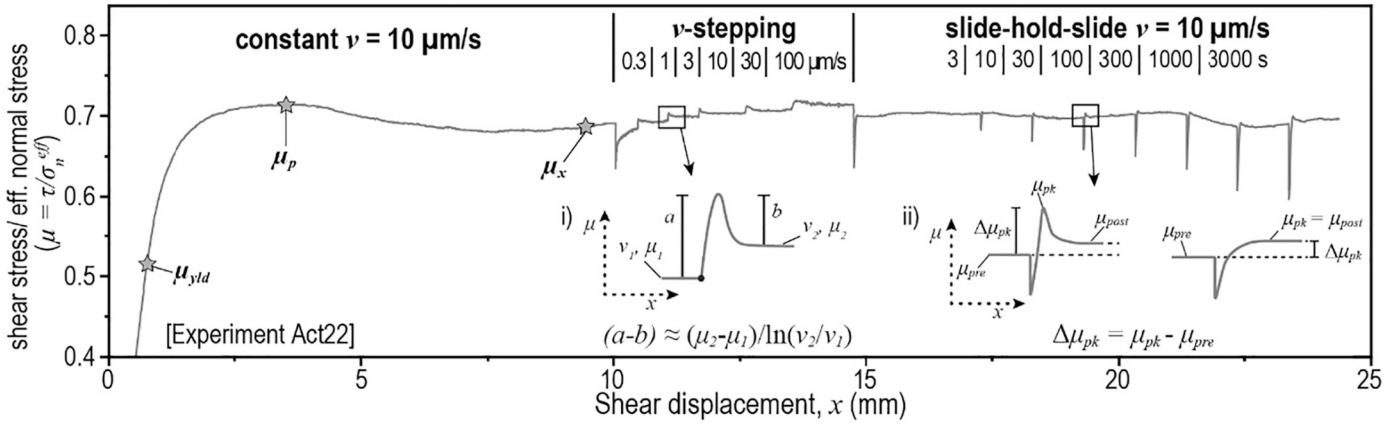

Fig. 4. Overview of the experimental approach and data analysis methods employed.

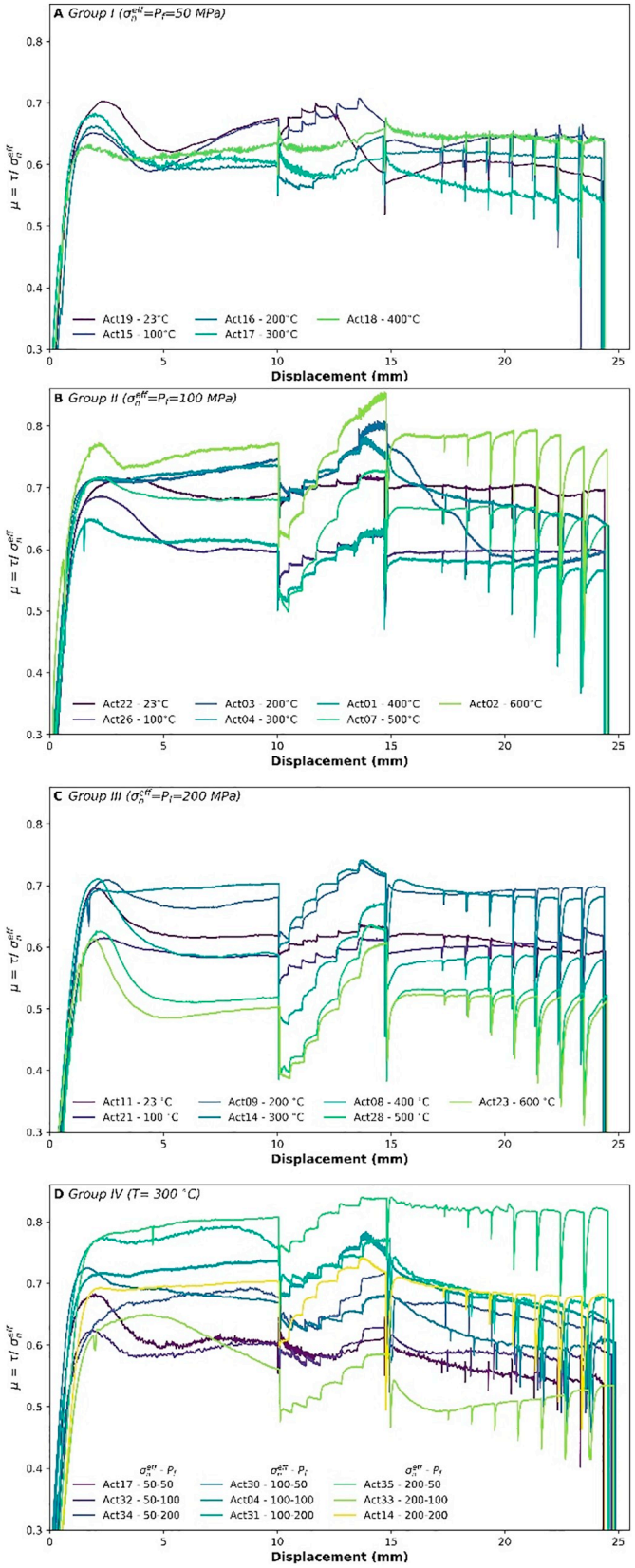

Fig. 5. Plots of friction coefficient against shear displacement, showing (representative) data from experiments from (A) Group I ($\sigma_n^{eff} = P_f = 50$ MPa), (B) Group II ($\sigma_n^{eff} = P_f = 100$ MPa), (C) Group III ($\sigma_n^{eff} = P_f = 200$ MPa), and (D) Group IV, including all conducted at $T = 300$ °C. See Table 1 for a list of all experiments and key parameters.

represent the targeted values used in each experiment, however, calculations of μ used the σ_n^{eff}-values corrected for seal friction. Shear displacement was corrected for elastic distortion of the machine. In presenting our data we picked shear stress (τ) and the apparent friction coefficient (μ), measured at $v = 10$ μm/s, at the 'apparent yield point' (resp. τ_{yld} and μ_{yld}), the maximum strength at low displacement ($x \leq 5$ mm; τ_p and μ_p), and at $x = 9.5$ mm (τ_x and μ_x) (Fig. 4). We define the 'apparent yield point' as the point of maximum deflection of the derivative of the μ vs. shear displacement (x) curve.

The velocity dependence of frictional strength was interpreted using the rate- and state-dependent friction (RSF) model (Dieterich, 1979),

$$\mu = \mu_0 + a\ln\left(\frac{v}{v_0}\right) + b\ln\left(\frac{v_0\theta}{d_c}\right) \text{with } \frac{d\theta}{dt} = 1 - \frac{v\theta}{d_c} \quad (1)$$

where μ_0 is the steady-state friction coefficient measured at a reference velocity v_0, characterized by an internal state $\theta(t)$. The parameters a and b are empirical constants that describe the magnitudes of, respectively, the instantaneous jump in μ that is observed upon a step-change in sliding velocity from v_0 to v, and the evolution effect, which describes transient adjustments that occur over a characteristic slip distance d_c required to re-attain steady-state sliding (see inset i. in Fig. 4; Marone, 1998a; Scholz, 1998). In the case of sliding at steady-state, $\dot{\theta} = 0$, and Eq. (1) yields

$$(a - b) = \frac{\partial \mu_{ss}}{\partial \ln v} \quad (2)$$

where $\Delta\mu_{ss}$ denotes the change in the steady-state coefficient of friction (μ_{ss}) before and after a perturbation in sliding velocity. Positive (a-b) values indicate v-strengthening behavior, which is intrinsically stable, whereas negative (a-b)-values indicate v-weakening which may lead to a state of unstable sliding (Ruina, 1983; Rice and Ruina, 1983). In the case of stable sliding, for each v-step we quantified the value of (a-b) and those of the individual parameters a, b and d_c, using an iterative least-squares fitting procedure (Reinen and Weeks, 1993; Ikari et al., 2009). Where applicable, we detrended the μ vs shear displacement data for linear slip hardening or softening trends (following Lockner et al., 1986). In the case of unstable sliding we estimated the value of (a-b) using the difference between the peak strengths ($\Delta\mu$) before and after a velocity step, i.e., assuming $(a\text{-}b) \approx \Delta\mu/\Delta\ln(v)$ (cf. He et al., 2003; Verberne et al., 2010). Slide-hold-slide data were analyzed by quantifying the difference between the coefficient of friction before the hold (μ_{pre}) and the peak strength achieved upon re-sliding (μ_{pk}), or $\Delta\mu_{pk} = \mu_{pk}$-$\mu_{pre}$ (see inset ii. in Fig. 4). The rate of fault healing is defined $\beta_{pk} = d(\Delta\mu_{pk})/d\log_{10}(t_{hold})$ (following Chen et al., 2015a).

Standard error propagation using $\delta\tau = \delta v = 0.1\%$ and $\delta\sigma_n^{eff} = 0.01\%$ shows that the relative error in (a-b) and $\Delta\mu_{pk}$ is respectively ~0.2% and ~0.14%. Note, however, that the standard deviation of (a-b)-values obtained from identical experiments on natural fault rocks is typically much larger than this measurement error, and can be on the order of 0.002–0.005, implying sample variability effects up to 50–100% - as shown by Niemeijer and Vissers (2014) in multiply repeated (5×) experiments on quartz-phyllosilicate-carbonate mixtures. Here, we tested variability of (a-b)- and $\Delta\mu_{pk}$-values by carrying out (multiple) repeat experiments (Table 1). For each experiment we quantified v-stepping as well as the SHS data, except in the case that the μ-x curve showed persistent displacement weakening or -hardening trends.

3. Results

3.1. Frictional strength data

A list of all experiments performed, the corresponding conditions, and key strength data is given in Table 1. We plot the apparent friction coefficient (μ) vs. shear displacement (x) for representative experiments

in Fig. 5. All experiments showed a rapid increase in friction coefficient in the first 1–2 mm of displacement, typically reaching an apparent yield point around $x \approx 1$ mm. Beyond $x \approx 10$ mm, (near-)steady-state values of the friction coefficient are usually observed (Fig. 5A–D), however, we observed some variability in the shape of μ vs. x curves, including between experiments performed at the same conditions. Specifically, some experiments showed persistent displacement-dependent hardening or weakening trends. In these cases, a third experiment was carried out, and the result which showed clearly anomalous behavior was omitted from subsequent analyses. This was found to be the case for experiments Act27 from Group I, Act05 from Group II, and Act13 and Act24 from Group III (refer μ-values in repeat experiments in Table 1). Unstable slip occurred in experiments conducted at $T = 300$ °C and 400 °C, at $\sigma_n^{eff} = P_f = 50$ MPa, at the lower sliding velocities employed ($v_2 \leq 30$ µm/s) (see inset Fig. 5A). For experiments from Group I and II (resp. $\sigma_n^{eff} = P_f = 100$ MPa and 200 MPa) we only observed stable sliding. In experiments conducted at $T = 300$ °C (Group IV), strength oscillations, indicative of unstable slip, were observed for $\sigma_n^{eff} = 50$ MPa and $P_f = 50$ MPa.

Values of μ_{yld}, μ_p, and μ_x observed in experiments from Groups I-III are plotted against temperature in Fig. 6A–C. The maximum spread in strength values for experiments from a given group at a single temperature was observed between experiments Act06 and Act22, carried out at 23 °C, and measured ~0.08 for μ_{yld}, ~0.06 for μ_p, and ~0.08 for μ_x. Within the scatter of the repeat experiments, there is little evidence for any systematic effects of temperature on μ_{yld}, μ_p, and μ_x (Fig. 6A–C), although an argument can made that the coefficient of friction at temperatures higher than 300 °C and 200 MPa normal stress is systematically lower than that at 100 MPa. Ignoring any variations of the friction coefficient with changing temperature, the average μ_{yld}-value, representative for all conditions tested, can be placed at $\mu_{yld} \approx 0.50$, with a standard deviation of ±0.05. Similarly, $\mu_p \approx 0.68 \pm 0.04$ and $\mu_x \approx 0.64 \pm 0.08$. The effects of changing λ on μ_{yld}, μ_p, and μ_x observed in experiments conducted at $T = 300$ °C, are shown in Fig. 6D. Little systematic variation is observed beyond the spread in μ-values.

3.2. Velocity dependence data

A list of all (a-b) data for each v-step is given in Table 2, with the results of the full inversion of the Dieterich-type rate-and-state-dependent constitutive equation given in Supplementary Table 1. The values of the rate-and-state parameters a, b and d_c change with temperature, effective normal stress, and sliding velocity. In general, the b parameter, which describes the evolution effect, shows a broad decrease to negative values with increasing temperature, increasing effective normal stress and decreasing velocity, which is mirrored by the value of d_c, that is, d_c increases with temperature, effective normal stress and a lower velocity. The a parameter, which describes the direct effect, shows less consistent changes, but generally increases with increasing effective normal stress. The (a-b)-values determined from v-stepping experiments from Groups I-III are plotted against temperature in Fig. 7. The maximum spread in (a-b)-values between experiments conducted at the same conditions is ~0.014. Values of (a-b) obtained in experiments from Group I ($\sigma_n^{eff} = P_f = 50$ MPa) are close to zero at all temperatures investigated, with a minimum around $T = 200$–400 °C for the lowest sliding velocities employed ($v_2 \leq 3$ µm/s) (Fig. 7A). For experiments from Group II and III (resp. $\sigma_n^{eff} = P_f = 100$ MPa and 200 MPa), the (a-b)-values increase with increasing temperature, with v-weakening or -neutral behavior occurring only at room temperature and at $T = 200$ °C (Fig. 7B, C).

To further elucidate the effects of sliding velocity and normal stress on (a-b)-values, we plot data for up-step sliding velocities (v_2) of 1 µm/s and 30 µm/s in Fig. 8. For $v_2 = 1$ µm/s, (a-b) shows a minimum value (negative) at 300 °C for experiments from Group I ($\sigma_n^{eff} = P_f = 50$ MPa), but an increasing trend with increasing temperature in experiments from Groups II and III (resp.

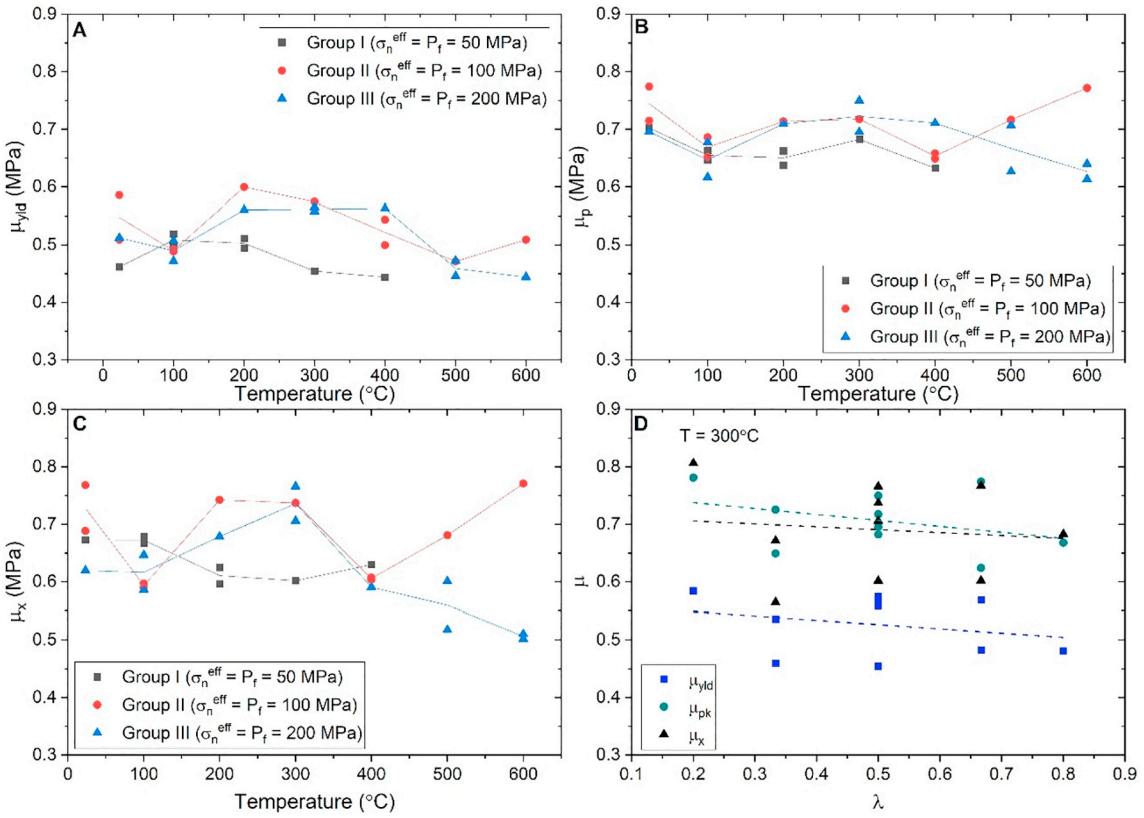

Fig. 6. Coefficient of friction at apparent yield (μ_{yld}), the peak-value at $x < 5$ mm (μ_p), and at x = 10 mm (μ_x), versus temperature (A–C) and pore fluid pressure ratio (λ) (D).

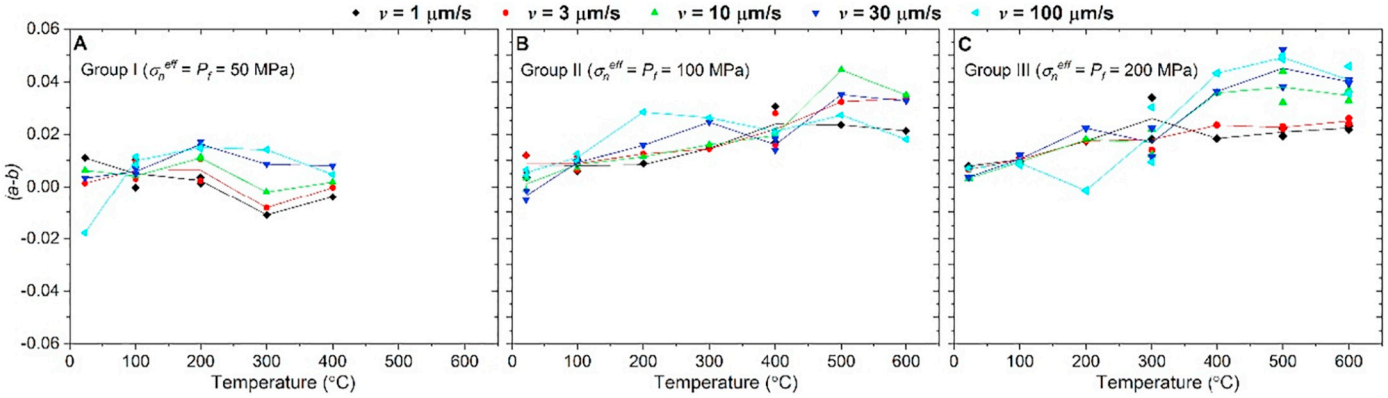

Fig. 7. Plots of (*a*-*b*) versus temperature for experiments of (A) Group I (($\sigma_n^{eff} = P_f$ = 50 MPa), (B) Group II ($\sigma_n^{eff} = P_f$ = 100 MPa), and (C) Group III ($\sigma_n^{eff} = P_f$ = 200 MPa).

$\sigma_n^{eff} = P_f$ = 100 MPa and 200 MPa) (Fig. 8A). For v_2 = 30 μm/s, the (*a*-*b*)-values show a maximum at ~200 °C for experiments from Group I, but a monotonic increase for Group II and III experiments over the entire temperature range investigated (Fig. 8B). The slope of the curve that interpolates mean values of (*a*-*b*) with increasing temperature is lower for v_2 = 1 μm/s compared with for v_2 = 30 μm/s (Fig. 8A, B).

Table 2
List of velocity-stepping data.

Experiment	*T* (°C)	σ_n^{eff} (MPa)	P_f (MPa)	(*a*-*b*) per *v*-step [in μm/s]				
				0.3 → 1	1 → 3	3 → 10	10 → 30	30 → 100
Group I: $\sigma_n^{eff} = P_f$ = 50 MPa (λ = 0.5)								
Act19	23	50	50	0.011	0.001	0.006	0.003	−0.018
Act15	100	50	50	0.010	0.010	0.004	0.007	0.011
Act27	100	50	50	0.011	0.014	0.005	0.011	0.011
u815	100	50	50	0.000	0.003	0.006	0.005	0.008
Act16	200	50	50	0.004	0.002	0.011	0.015	0.014
Act25	200	50	50	0.001	0.010	0.011	0.017	0.016
Act17	300	50	50	−0.011	−0.008	−0.002	0.009	0.014
Act18	400	50	50	−0.004	0.000	0.002	0.008	0.005
Group II: $\sigma_n^{eff} = P_f$ = 100 MPa (λ = 0.5)								
Act06	23	100	100	0.012	0.012	−0.001	−0.005	0.000
Act22	23	100	100	0.004	0.006	0.003	−0.001	0.004
Act05	100	100	100	0.010	0.004	0.007	0.012	0.014
Act26	100	100	100	0.010	0.011	0.010	0.010	0.013
u821	100	100	100	0.006	0.006	0.007	0.009	0.010
Act03	200	100	100	0.009	0.013	0.012	0.016	0.028
Act04	300	100	100	0.015	0.014	0.016	0.025	0.026
Act01	400	100	100	0.017	0.016	0.020	0.018	0.020
Act20	400	100	100	0.031	0.028	0.019	0.014	0.022
Act07	500	100	100	0.024	0.032	0.044	0.035	0.027
Act02	600	100	100	0.021	0.034	0.035	0.033	0.018
Group III: $\sigma_n^{eff} = P_f$ = 200 MPa (λ = 0.5) (λ = 0.5)								
Act11	23	200	200	0.008	0.007	0.003	0.004	0.007
Act21	100	200	200	0.011	0.009	0.008	0.010	0.012
Act29	100	200	200	0.011	0.009	0.010	0.010	0.010
Act09	200	200	200	0.017	0.018	0.018	0.022	−0.001
Act14	300	200	200	0.034	0.022	0.022	0.022	0.030
u822	300	200	200	0.018	0.014	0.012	0.012	0.009
Act08	400	200	200	0.018	0.023	0.036	0.036	0.043
Act12	500	200	200	0.019	0.022	0.032	0.038	0.050
Act28	500	200	200	0.022	0.023	0.044	0.052	0.048
Act10	600	200	200	0.022	0.024	0.033	0.041	0.046
Act23	600	200	200	0.023	0.026	0.037	0.039	0.036
Group IV: Constant *T* = 300 °C (λ = 0.2 to 0.8)								
Act32	300	50	100	−0.002	0.009	0.011	0.015	0.018
Act34	300	50	200	0.004	0.003	0.013	0.020	0.020
Act30	300	100	50	0.009	0.016	0.015	0.019	0.019
Act31	300	100	200	0.013	0.013	0.021	0.018	0.023
Act35	300	200	50	0.013	0.016	0.021	0.010	0.008
Act33	300	200	100	0.012	0.014	0.030	0.027	0.017

T = temperature; σ_n^{eff} = normal stress; P_f = pore fluid pressure; $\lambda = P_f/\sigma_n = P_f/(\sigma_n^{eff} + P_f)$ = pore fluid pressure ratio. See Supplementary Table 1 for a list of the full inversion of a Dieterich-type RSF equations, incl. parameters *a*, *b*, d_c.

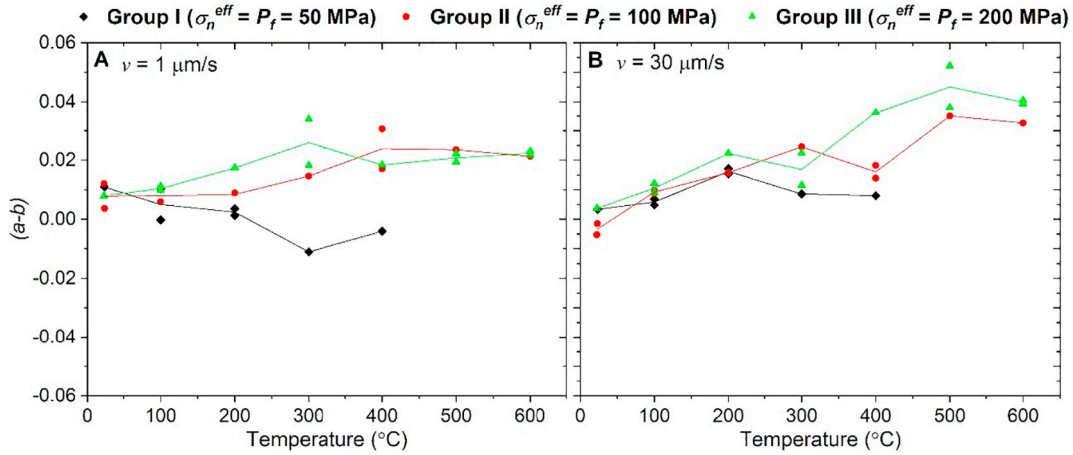

Fig. 8. Plots of (*a*-*b*) versus temperature for (A) data for the *v*-step from 0.3 to 1 μm/s, and (B) 1 to 30 μm/s.

3.3. Slide-hold-slide data

A list of all strength values from slide-hold-slide experiments (μ_{pre}, μ_{pk}, $\Delta\mu_{pk}$ – ref. Fig. 4) is given in Supplementary Table 2. We plot $\Delta\mu_{pk}$-values from each experiment against log(t_{hold}) in Fig. 9. Experiments from Group I ($\sigma_n^{eff} = P_f = 50$ MPa) carried out at $T = 100$–300 °C show a log-linear correlation between $\Delta\mu_{pk}$ and hold time, compared with $\Delta\mu_{pk} \approx 0$ regardless of t_{hold} for $T = 23$ °C and 400 °C (Fig. 9A). All experiments from Group II ($\sigma_n^{eff} = P_f = 100$ MPa) showed little trend with t_{hold} beyond the experimental variability, except for $t_{hold} = 1000$–3000 s, which shows an increase of $\Delta\mu_{pk}$. Apparent negative $\Delta\mu_{pk}$-values are also observed, but the absolute values are very small and within the range of experimental variability (i.e., $|\Delta\mu_{pk}| \leq 0.01$) (Fig. 9B). Experiments from Group III ($\sigma_n^{eff} = P_f = 200$ MPa) carried out using $T = 100$ °C and 600 °C showed an increase of $\Delta\mu_{pk}$ with increasing hold time for $t_{hold} \geq 30$ s, whereas experiments at all other temperatures tested (23 °C, 200–500 °C) showed little or no variation in $\Delta\mu_{pk}$ (Fig. 9C). All experiments conducted at 300 °C showed an increase of $\Delta\mu_{pk}$ for $t_{hold} = 1000$–3000 s, whereas a near log-linear increase spanning all explored hold times is observed in tests conducted at $\sigma_n^{eff} = 50$ MPa and $P_f \leq 100$ MPa. The rate of fault healing ranged from $\beta_{pk} \approx 0.009$/decade in experiment u821 to $\beta_{pk} \approx 0.017$/decade in experiments Act16 and Act25 (ref. Fig. 9).

3.4. Microstructures

Sample fragments recovered after an experiment were generally

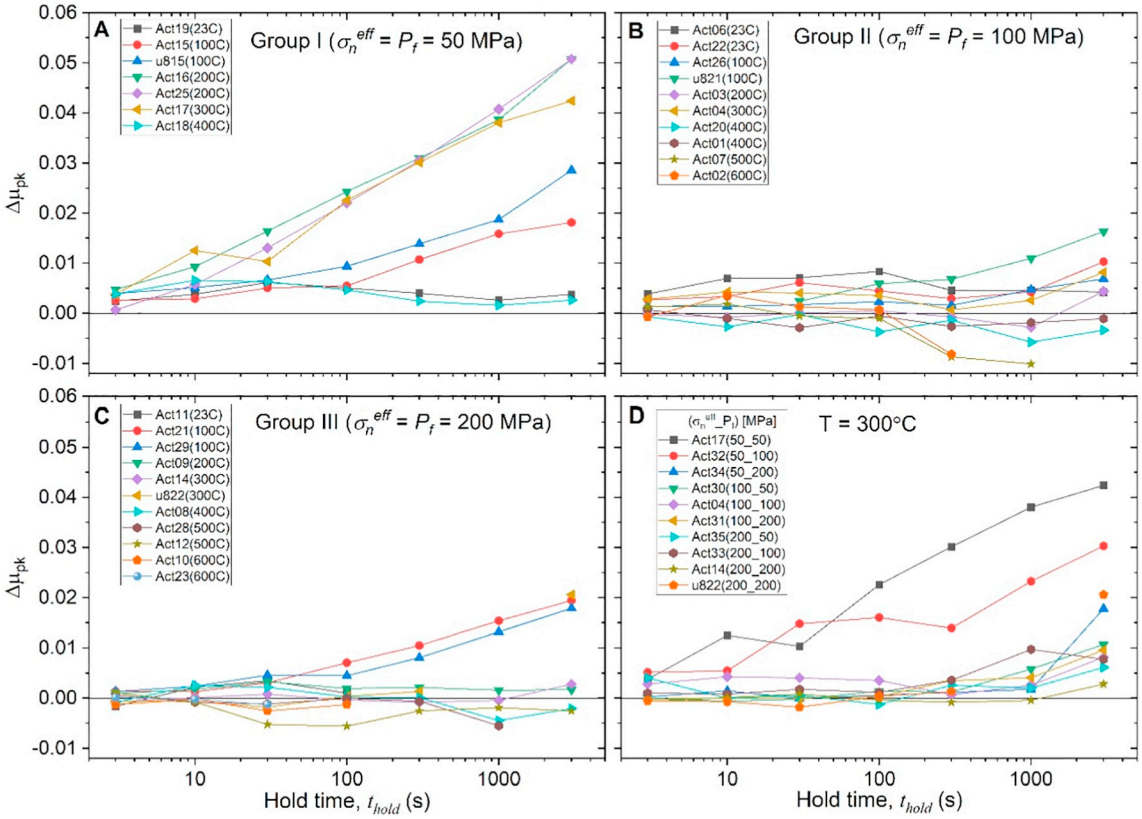

Fig. 9. Data from slide-hold-slide experiments, plotted as $\Delta\mu_{pk}$ versus hold time. A) Group I ($\sigma_n^{eff} = P_f = 50$ MPa), (B) Group II ($\sigma_n^{eff} = P_f = 100$ MPa), (C) Group III ($\sigma_n^{eff} = P_f = 200$ MPa, and (D) Group IV, including all experiments conducted at $T = 300$ °C.

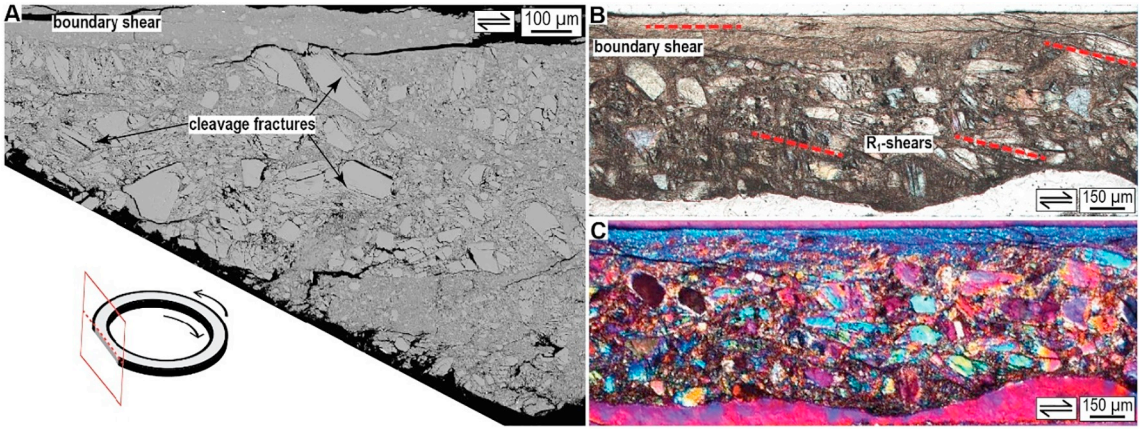

Fig. 10. Microstructures of recovered fragments. A) Backscattered electron micrograph (experiment Act06 - $\sigma_n^{eff} = P_f = 100$ MPa, $T = 23$ °C). B) Plane polarized and C) cross-polarized light micrographs (experiment Act07 - $\sigma_n^{eff} = P_f = 100$ MPa, $T = 500$ °C).

very small, which prevented systematic investigation of post-mortem microstructure. Regardless, few recovered fragments showed potentially important microstructural features, which are represented by the micrographs shown in Fig. 10. The sectioned fragments shown here were recovered from experiments Act06 and Act07, respectively sheared at room temperature and at 500 °C (Table 1).

Samples Act06 and Act07 both show evidence for a ~100–200 µm wide, shear-plane parallel band of (ultra-)finely comminuted grains cutting a coarser-grained bulk sample (Fig. 10A, B), indicating localized shear deformation in a boundary shear band. From the sample sheared at room temperature (sample Act06), observed using BSE (Fig. 10A), the maximum grain size (long axis) within the boundary shear is ~30–40 µm, compared with ~150–200 µm in the bulk sample where the larger grains are characterized by widespread cleavage fractures. When viewed in cross-polarized light, the boundary shear formed at 500 °C (sample Act07) shows a uniform birefringence and optical extinction (Fig. 10C), which is strongly suggestive of a crystallographic preferred orientation (CPO) (cf. Verberne et al., 2013; Niemeijer, 2018). The boundary shear band and the bulk sample are itself cut by fractures inclined at an angle of ~15–20° to the shear direction (Fig. 10B), which are reminiscent of R_1-shears (terminology of Logan et al., 1979). In the case of amphibole, a CPO implies a shape preferred orientation (SPO) because each grain has a columnar shape with a long axis parallel to the *c*-axis. The SPO equivalent to CPO is frequently observed in naturally deformed actinolite aggregates (cf. Fig. 1C, D), and may be formed by either preferential nucleation and growth of amphibole in the *c*-axis orientation or by rigid-body rotation in a ductile matrix (e.g., Imon et al., 2004).

4. Discussion

4.1. Reproducibility of friction coefficient data

Despite using identical conditions of (effective) normal stress (σ_n^{eff}), pore fluid pressure (P_f), and temperature (T) in repeat experiments, the values of the friction coefficient that we measured at a shear displacement of 9.5 mm (μ_x) was observed to vary significantly in some cases. For example, in experiments Act14 and Act24, carried out at $\sigma_n^{eff} = P_f = 200$ MPa and $T = 300$ °C, we measured respectively $\mu_x = 0.71$ and 0.51, whereas in experiments Act01 and Act20, carried out using $\sigma_n^{eff} = P_f = 100$ MPa and $T = 400$ °C, we measured respectively 0.61 and 0.60 (Table 1). A third experiment at $\sigma_n^{eff} = P_f = 200$ MPa and $T = 300$ °C (u822) showed $\mu_x = 0.77$, suggesting that experiment Act24 showed an anomalously low μ_x-value. In experiment Act24, we observed strong displacement-weakening, which was absent in the other two experiments performed under identical conditions. One possible explanation for this contrasting behavior might be found in the nature of the low-friction coating of the confining rings. This coating was applied manually using a brush in all original experiments, while a spray coating was used in the recent repeat experiments (u815, u821, u822). We speculate that the quality of the coating used in experiment Act24 was poor, with relatively large variations in thickness on the confining rings. This can lead to scraping-off of the coating, and subsequent incorporation into the sample layer, effectively reducing its frictional strength. Ignoring repeat experiments that had clear anomalous behavior of strong displacement weakening or hardening trends improved the reproducibility dramatically, with, in the worst case, a spread in μ_x–values of 0.08.

Furthermore, in the present experiments we cannot rule out some effect of variability in seal friction. Based on previous work we expect that these effects are small, specifically, <10% of the seal friction, but at the lowest effective normal stress of 50 MPa this could give rise to a variation in friction of up to ±0.01. Another possibility is that during initial sliding at 10 µm/s the fault gouge becomes disconnected or poorly connected to the fluid reservoir due to shear-enhanced compaction (Faulkner et al., 2018). This would lead to the variable development of a high(er) internal pore fluid pressure and lower effective normal stress, leading to apparent weakening. It is reasonably to suggest that the (permeability of the) localized shear bands characterized by a CPO/SPO, observed in recovered fragments (Fig. 10), has some role to play in effectively 'sealing' the sample from the pore fluid reservoir. However, the detailed reasons for limited reproducibility and slip hardening and weakening effects seen in our experiments remain subject of further investigation.

4.2. Effects of experimental variables on the friction coefficient and healing

Even though there is considerable experimental variability in the measured friction, we do observe some changes in friction with temperature that go beyond this variability, in particular in the value of the coefficient of friction at (near-)steady state sliding, μ_x. For high normal stress and fluid pressure experiments (Group III), friction increases monotonically with increasing temperature up to 300 °C, reaching μ_x of 0.74 ± 0.03. At higher temperatures, friction decreases reaching μ_x of 0.51 at 600 °C. By contrast, experiments at the intermediate normal stress and fluid pressure (Group II) shows little systematic variation in friction up to 300 °C. Friction then drops to μ_x of 0.605 ± 0.005 at $T = 400$ °C and increases monotonically to μ_x of 0.77 at $T = 600$ °C. By comparison, in hydrothermal ring shear experiments using simulated gouges composed of illite-quartz and muscovite-quartz mixtures (Den Hartog et al., 2012b, 2013), the μ-value measured at the final displacement ($x_{fnl} \geq 40$ mm) was reported to increase from ~0.55–0.60 to

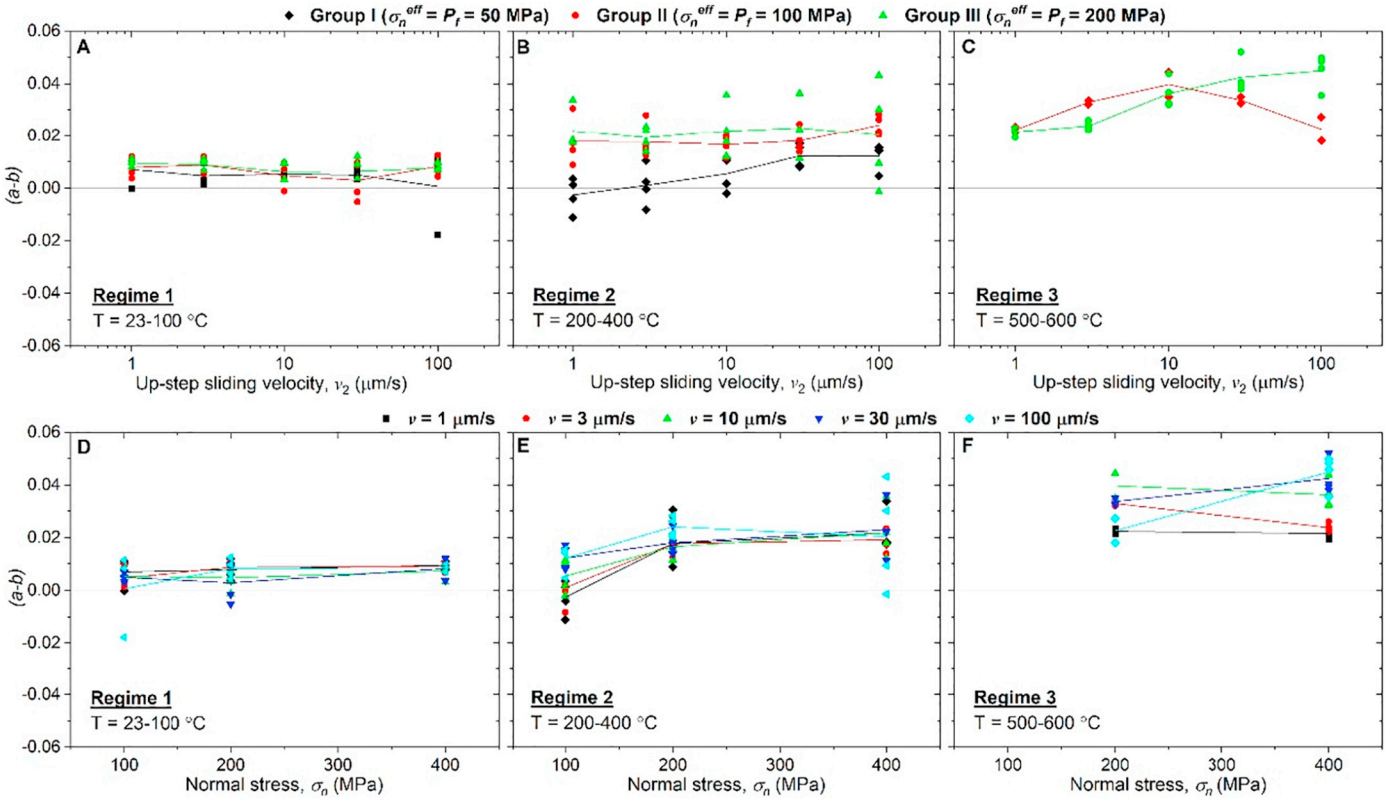

Fig. 11. The velocity-dependence (*a-b*) versus log sliding velocity (A to C), and versus normal stress (D to F), for experiments conducted using λ = 0.5, at temperatures of 23–100 °C (Regime 1: A and D), 200–400 °C (Regime 2: B and E), and 500–600 °C (Regime 3: C and F).

~0.80–0.95 over a temperature range from 100 °C to 500 °C. The small effect of temperature on the friction coefficient of Act:Chl gouge mixtures seen in the present experiments (Fig. 6A–C) are more in line with data from experiments using gouges of mafic compositions. Specifically, hydrothermal friction experiments using simulated gouges composed of gabbro (He et al., 2007) and basalt (Zhang et al., 2017) show an increase of final μ-value ($x_{fnl} \approx$ 2–4 mm) from 0.70 to 0.74 in the temperature range from 21 °C to ~600 °C, and mafic gouges (>50% hornblende + plagioclase + quartz) tested by Hellebrekers et al. (2019) showed μ = 0.67 to 0.72 at T = 22–700 °C.

Data from slide-hold-slide (SHS) experiments are widely used to study fault healing effects, which may strongly influence earthquake nucleation, magnitude, and recurrence interval (see e.g., Marone et al., 1995; Marone, 1998a, 1998b; Carpenter et al., 2011; Chen et al., 2015a,b). Our SHS tests on sheared simulated Act-Chl faults showed striking differences between experiments carried out at different σ_n^{eff}-P_f conditions (i.e., within a single group – see Fig. 9, Table 1, and Supplementary Table 2). Experiments conducted at 100–300 °C from Group I ($\sigma_n^{eff} = P_f$ = 50 MPa), and at 100 °C from Groups II and III (resp. $\sigma_n^{eff} = P_f$ = 100 MPa and 200 MPa) showed a marked, near-loglinear increase in $\Delta\mu_{pk}$ with t_{hold} (cf. Dieterich, 1979), compared with no visible trend beyond the experimental variability for all other experiments from Groups I-III (Fig. 9). Experiments carried out at 300 °C, including those within Group IV, showed loglinear healing only for σ_n^{eff} = 50 MPa (Fig. 9D). Fault re-strengthening or healing upon piston hold is generally attributed to compaction or densification of the (initially porous) sample, by time-sensitive deformation processes such as pressure solution (Yasuhara et al., 2005; Tenthorey and Cox, 2006; Chen et al., 2015a,b). Our results do not show a consistent increase of $\Delta\mu_{pk}$, or of β_{pk}, with increasing temperature. To our knowledge, little data exists on time-dependent deformation of granular actinolite aggregates, let alone in the presence of chlorite. For this reason, and for to the lack of preserved microstructures, the underlying mechanism controlling healing in our experiments remains enigmatic. The variable development of internal pore fluid pressure, combined with the presence of fine-grained shear bands characterized by a CPO/SPO (Fig. 10), mentioned above may also have played a role here.

4.3. Effects of experimental variables on (a-b)

We observed variations of the v-dependence parameter (*a-b*) with increasing temperature (T), effective normal stress (σ_n^{eff}), pore fluid pressure (P_f), as well as with changes in the (up-step) sliding velocity (v_2) (Figs. 7, 8). Most experiments showed v-strengthening behavior characterized by (*a-b*) > 0, however v-weakening ((*a-b*) < 0) was observed in experiments conducted at T = 300–400 °C (Table 2, Supplementary Table 1). Measurements of shear stress upon changes in shear displacement rate, which are used to calculate (*a-b*) values, may have been affected by transient changes in pore fluid pressure (Ikari et al., 2009; Niemeijer et al., 2016; Faulkner et al., 2018), especially in view of the expected low permeability of sheared phyllosilicate gouges (Takahashi et al., 2007; Carpenter et al., 2014). However, following Ikari et al. (2009), we expect that the effect of this on (*a-b*) is small - especially when compared with sample variability effects, which may be up to 50–100% (Niemeijer and Vissers, 2014), and considering the long duration of the slowest velocity steps compared with the characteristic diffusion time (see Faulkner et al., 2018). Therefore, we ignore any effects of transient pore fluid overpressure on the values of (*a-b*).

Combining v-stepping data from all experiments conducted using λ = 0.5, and $\sigma_n^{eff} = P_f$ = 50, 100, or 200 MPa, the effects of sliding velocity and normal stress ($\sigma_n = \sigma_n^{eff} + P_f$) on (*a-b*)-value can be divided into three temperature regimes (Fig. 11). In Regime (1), characterized by T = 100 °C or less, (*a-b*) remains constant with increasing v_2, and does not vary with σ_n changing in the range from 100 MPa to 400 MPa (Fig. 11A, D). In Regime (2), T = 200–400 °C, (*a-b*) increases

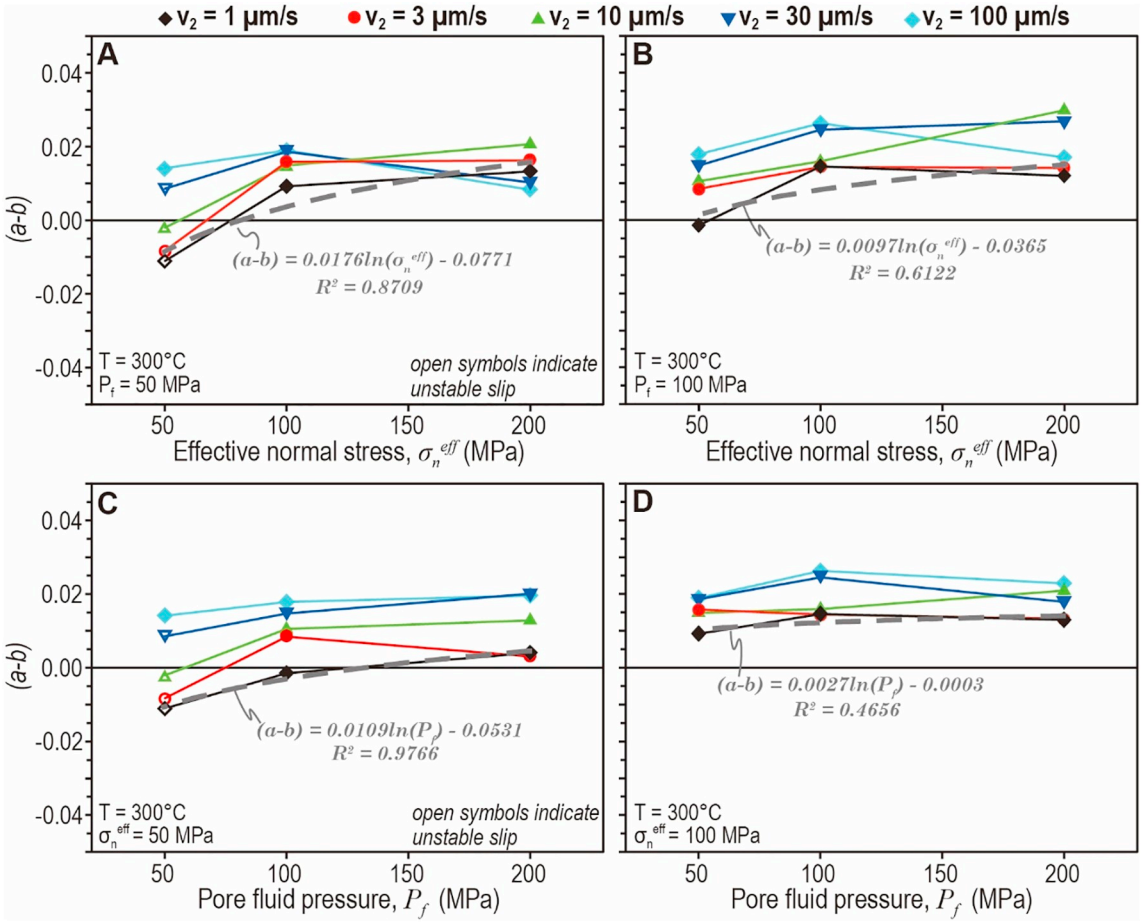

Fig. 12. The velocity dependence (*a*-*b*) plotted against effective normal stress (A and B) and pore fluid pressure (C and D). Data from experiments conducted at 300 °C. Dashed grey lines show logarithmic fits, along with the resulting formula and the goodness-of-fit value (R^2).

with increasing v_2. In this regime (*a*-*b*) is negative only at 300 °C, at low v_2 and at low σ_n but otherwise positive. It increases with increasing normal stress between σ_n = 100 MPa and 200 MPa, but no change in (*a*-*b*) occurs between σ_n = 200 MPa and 400 MPa (Fig. 11B, E). In Regime (3), T = 500 °C and above, (*a*-*b*) is positive at σ_n = 200 and 400 MPa. Here, the effects of sliding velocity and normal stress are not clear-cut (Fig. 11C, F), partly because we do not have data for σ_n = 100 MPa ($\sigma_n^{eff} = P_f$ = 50 MPa). Nonetheless, an increasing trend in (*a*-*b*) with increasing v_2 is observed for σ_n = 400 MPa (Fig. 8C). We note that the temperature marking the boundary between Regimes (1) and (2), at around 200 °C, is close to the lower limit of the stability field of actinolite, when actinolite starts to form during metamorphism of mafic protolith. The temperature marking the boundary between Regimes (2) and (3), around 400–500 °C, may be related to the oxidation of ferric iron in actinolite (Ernst, 1966; Jenkins and Bozhilov, 2003). Although we lack post-mortem compositional data, we expect that reaction kinetics are not fast enough in the short duration of our experiments.

Within Regime 2, the value of (*a*-*b*) shows a minimum for T = 300–400 °C and σ_n = 100 MPa ($\sigma_n^{eff} = P_f$ = 50 MPa) (Figs. 7A, 11B, E). Minima of (*a*-*b*)-values with increasing temperature have been reported for a wide range of (simulated) gouge types deformed in hydrothermal shear tests, including for granite (Blanpied et al., 1991, 1995), gabbro (He et al., 2007), illite-quartz mixtures (Den Hartog et al., 2012b), calcite (Verberne et al., 2015), chlorite-rich mylonite (Zhang and He, 2016), and chlorite (Okamoto et al., 2019). Den Hartog and Spiers (2013) suggested that the observed effects of temperature on (*a*-*b*) in illite-quartz gouge are caused by the competition between gouge compaction involving pressure solution of quartz clasts and dilatant frictional slip on the intervening phyllosilicates (following Niemeijer and Spiers, 2006). Although there is no quartz in the samples studied here, pressure solution of actinolite and/or chlorite might provide an explanation for the temperature-dependence of (*a*-*b*) similar to that of illite-quartz gouge.

Velocity-stepping data from experiments conducted at T = 300 °C, using λ = 0.2 to 0.8, show that both σ_n^{eff} and P_f may affect (*a*-*b*) values (Fig. 12A–D). The value of (*a*-*b*) increases with increasing σ_n^{eff} regardless of the P_f-value used (Fig. 12A, B), whereas it increases with increasing P_f but only for σ_n^{eff} = 50 MPa (Fig. 12C). For σ_n^{eff} = 100 MPa, P_f seems not to affect the (*a*-*b*)-value (Fig. 12D). Best-fit trends to the data are suggestive of a logarithmic increase of (*a*-*b*) with increasing

Table 3
Results of multiple regression using $(a\text{-}b) = b_0 + b_1 \ln(\sigma_n^{eff}) + b_2 \ln(P_f)$.

	Result	Goodness of fit (adjusted R^2)	Standard error (of regression)	Test values
b_0	−0.10880	0.78014	SE = 0.00580	F-value: 0.00448
b_1	0.01625	n/a	SER = 0.78944	t-Value: 4.76196 (p-value = 0.00312)
b_2	0.00948	n/a	SER = 0.46031	t-Value: 2.77666 (p-value = 0.03214)

SE = standard error. SER = standard error of regression. For details see e.g. Wonnacott and Wonnacott (1990).

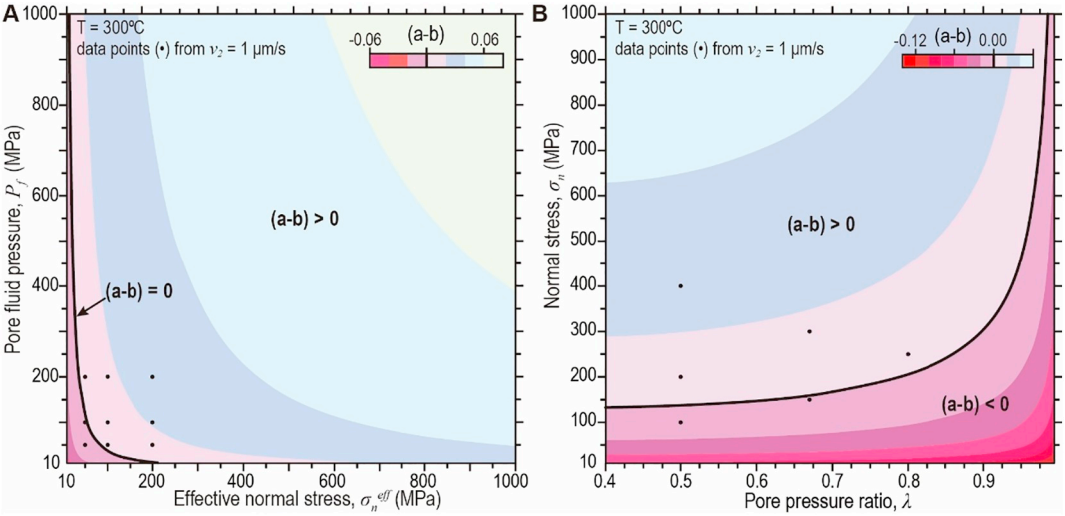

Fig. 13. Contour maps of (*a*-*b*), generated using multiple regression analysis of data from experiments conducted at 300 °C (black dots). (A) Pore fluid pressure versus effective normal stress. (B) Normal stress versus pore pressure ratio.

σ_n^{eff} or P_f, especially for the lower sliding velocities employed. Comparison of the slopes of the best-fit curves shown in Fig. 12A, B versus Fig. 12C, D suggests that the (*a*-*b*)-values are more sensitive to σ_n^{eff} than to P_f.

4.4. The role of λ and implications for subduction zone seismogenesis

To further investigate how (*a*-*b*) depends on σ_n^{eff} and P_f, as well as to enable extrapolation of our results to conditions outside the present experiments, we performed multiple regression analysis on data of (*a*-*b*) vs σ_n^{eff} and P_f. We used data obtained at the lowest sliding velocities employed (i.e., stepping from 0.3 μm/s to 1 μm/s) because these are closest to the displacement rate of subducting oceanic plate (~1 nm/s - Segall and Rice, 2006). As shown in Fig. 12A–D, we interpreted our data to reflect a logarithmically increasing trend, assuming the form

$$(a-b) = b_0 + b_1 \ln(\sigma_n^{eff}) + b_2 \ln(P_f) \quad (3)$$

where b_0, b_1, and b_2 are constants. Regression results, including the standardized regression coefficient, and *f*-, *t*-, *p*-values describing the fit quality (see e.g., Wonnacott and Wonnacott, 1990), are listed in Table 3. Since $p < 0.005$ for both σ_n^{eff} and P_f, this suggests that that regression is statistically significant at the 95% confidence level. Since the standardized regression coefficient for σ_n^{eff} ($b_1 \approx 0.79$) is larger than that of P_f ($b_2 \approx 0.46$) this suggests that (*a*-*b*) is more sensitive to changes in σ_n^{eff} than to changes in P_f (consistent with the visual trends seen in Fig. 12A–D). Lastly, the adjusted coefficient of determination (R^2) is 0.78, with $F \approx 0.0045$, suggesting a reasonable fit of Eq. (3) to our data.

Using Eq. (3) and the results of multiple regression (Table 3) we plot a contour map for (*a*-*b*) in P_f-σ_n^{eff} space in Fig. 13A. The result suggests that a relatively high pore fluid pressure combined with relatively low effective normal stress promotes negative (*a*-*b*) values hence potentially unstable fault slip in simulated Act:Chl faults. To investigate this further, we rewrite Eq. (3) using the pore pressure ratio $\lambda = P_f/\sigma_n$ as

$$(a-b) = b_0 + \ln\{(1-\lambda)^{b_1} \bullet \lambda^{b_2}\} + \ln(\sigma_n^{(b_1+b_2)}) \text{with } \lambda = \frac{P_f}{\sigma_n} \quad (4)$$

We used Eq. (4) to plot a contour map for (*a*-*b*) in σ_n-λ space (Fig. 13B). The contour map shows that, under hydrostatic conditions ($\lambda \approx 0.4$) in a fault zone cutting actinolite-chlorite rich rocks, unstable slip is expected to occur at normal stresses below ~150 MPa (Fig. 13B). Furthermore, our empirical fit suggests that a high pore pressure ratio of >0.9 may promote potentially unstable fault-slip at higher normal stresses/greater depths. This is consistent with inferences made from field studies of fossilized subduction zones (Ujiie et al., 2018; Tarling et al., 2019), as well as with seismological observations (Kodaira et al., 2004; Audet et al., 2009; Peacock et al., 2011). However, these conditions were not experimentally tested in our study so this needs to be confirmed in future studies, preferably including a mechanism-based understanding for a decrease in (*a*-*b*) with increasing pore fluid pressure ratio λ.

5. Conclusions

We performed frictional sliding experiments on actinolite (Act, ~85%) + chlorite (Chl, ~15%) gouge mixtures under hydrothermal conditions using a ring shear apparatus. Experiments were performed at temperatures (T) of 23–600 °C, effective normal stresses (σ_n^{eff}) of 50–200 MPa and pore fluid pressures (P_f) of 50–200 MPa, employing shear displacement rates (v) in the range from 0.3 to 100 μm/s. Shear stress (τ) data were analyzed using the apparent coefficient of friction ($\mu = \tau/\sigma_n^{eff}$), data from *v*-stepping tests were analyzed using the rate-and-state parameter (*a*-*b*), and data from slide-hold-slide tests were analyzed to investigate fault healing ($\Delta\mu_{pk}$) with hold time. Our conclusions are as follows:

(1) Most experiments showed steady-state μ-values between 0.5 and 0.8, with some experiments showing displacement-weakening or -hardening. The variation in friction with temperature is smaller than the variability seen between experiments performed under identical conditions, implying that any effect of temperature on friction coefficient could not be reliably determined.
(2) Stable velocity-strengthening behavior ((*a*-*b*) > 0) was observed in all experiments conducted at $\sigma_n^{eff} = P_f = 100$–200 MPa, at all temperatures and displacement rates investigated. The value of (*a*-*b*) increased with increasing temperature. In experiments performed at $\sigma_n^{eff} = P_f = 50$ MPa, we found (near-)velocity-neutral behavior ((*a*-*b*) = 0), and velocity-weakening ((*a*-*b*) < 0) in the temperature range from 300 °C to 400 °C for the lower displacement rates employed (v = 0.3–3 μm/s).
(3) Effects of sliding velocity and normal stress on (*a*-*b*)-values varied with temperature. We identified three *T*-regimes. In Regime 1, from room temperature to 100 °C, (*a*-*b*) is independent of v and σ_n. In Regime 2, between 200 °C and 400 °C, (*a*-*b*) increases steadily with increasing v. At T = 300 °C in this regime, we found that the value of (*a*-*b*) increases with both σ_n^{eff} and P_f, in a roughly logarithmic

manner, especially where determined in v-steps from 0.3 to 1 μm/s. In Regime (3), above 500 °C, we observed no clear trend in the data.

(4) Extrapolation of our results on the effects of σ_n^{eff} and P_f on (a-b), using multiple regression, suggests that potentially unstable, velocity-weakening behavior in faults cutting Act:Chl compositions is limited to low effective normal stress conditions at a temperature of 300 °C.

Supplementary data to this article can be found online at https://doi.org/10.1016/j.tecto.2020.228377.

Author contributions

A. S. Okamoto: Conceptualization, Methodology, Software, Validation, Formal analysis, Investigation, Resources, Data Curation, Writing (original draft), Visualization, Project Administration, Funding Acquisition.

A. R. Niemeijer: Methodology, Validation, Investigation, Writing (review and editing), Supervision, Formal Analysis.

T. Takeshita: Conceptualization, Funding acquisition, Writing (review and editing), Supervision, Project Administration, Resources.

B. A. Verberne: Writing (review and editing), Formal Analysis, Visualization, Project Administration.

C. J. Spiers: Project Administration, Supervision, Resources, Writing (review and editing).

Declaration of competing interest

The authors declare that they have no known competing financial interests or personal relationships that could have appeared to influence the work reported in this paper.

Acknowledgments

We thank Tony van der Gon-Netscher, Gert Kastelein, Eimert de Graaff and Peter van Krieken for technical support, and Ichiko Shimizu for fruitful discussions. The first author thanks S. den Hartog for her advice when using the ring shear apparatus at Utrecht University. Changrong He and Brett Carpenter are thanked for constructive reviews which improved the final manuscript. This study was funded by JSPS KAKENHI grant #13J03294 awarded to ASO. ARN was supported by the Netherlands Organisation for Scientific Research (NWO) through VIDI grant nr. 854.12.011 and by ERC starting grant SEISMIC (nr. 335915). TT was supported by JSPS KAKENHI grant #26109004, and BAV by JSPS KAKENHI grant #19K14823.

References

Audet, P., Bostock, M.G., Christensen, N.I., Peacock, S.M., 2009. Seismic evidence for overpressured subducted oceanic crust and megathrust fault sealing. Nature 457, 76–78.

Bebout, G.E., 2007. Metamorphic chemical geodynamics of subduction zones. Earth Planet. Sci. Lett. 260, 373–393.

Bebout, G.E., Barton, M.D., 2002. Tectonic and metasomatic mixing in a high-T, subduction-zone mélange – insights into the geochemical evolution of the slab-mantle interface. Chem. Geol. 187, 79–106.

Blanpied, M.L., Lockner, D.A., Byerlee, J.D., 1991. Fault stability inferred from granite sliding experiments at hydrothermal conditions. Geophys. Res. Lett. 18, 609–612.

Blanpied, M.L., Lockner, D.A., Byerlee, J.D., 1995. Frictional slip of granite at hydrothermal conditions. J. Geophys. Res. 100, 13045–13064.

Boulton, C., Niemeijer, A.R., Hollis, C.J., Townend, J., Raven, M.D., Kulhanek, D.K., Shepherd, C.L., 2019. Temperature-dependent frictional properties of heterogeneous Hikuranging Subduction Zone input sediments, ODP Site 1124. Tectonophysics 757, 123–139.

Brown, J.R., Beroza, G.C., Ide, S., Ohta, K., Shelly, D.R., Schwartz, S.Y., Rabbel, W., Thorwart, M., Kao, H., 2009. Deep low-frequency earthquakes in tremor localize to the plate interface in multiple subduction zones. Geophys. Res. Lett. 36, L19306. https://doi.org/10.1029/2009GL040027.

Carpenter, B.M., Marone, C., Saffer, D.M., 2011. Weakness of the San Andreas Fault revealed by samples from the active fault zone. Nat. Geosci. 4, 251–254.

Carpenter, B.M., Kitajima, H., Sutherland, R., Townend, J., Toy, V.G., Saffer, D.M., 2014. Hydraulic and acoustic properties of the active Alpine Fault, New Zealand: laboratory measurements on DFDP-1 drill core. Earth Planet. Sci. Lett. 390, 45–51.

Chen, J., Verberne, B.A., Spiers, C.J., 2015a. Interseismic re-strengthening and stabilization of carbonate faults by "non-Dieterich-type" healing under hydrothermal conditions. Earth Planet. Sci. Lett. 423, 1–12.

Chen, J., Verberne, B.A., Spiers, C.J., 2015b. Effects of healing on the seismogenic potential of carbonate fault rocks: experiments on samples from the Longmenshan Fault, Sichuan, China. J. Geophys. Res. 120, 5479–5506.

Chernak, L.J., Hirth, G., 2011. Syndeformational antigorite dehydration produces stable fault slip. Geology 39, 847–850.

Christensen, N.I., Salisbury, M.H., 1975. Structure and constitution of the lower oceanic crust. Rev. Geophys. Space Ge. 13, 57–86.

Den Hartog, S.A.M., Spiers, C.J., 2013. Influence of subduction zone conditions and gouge composition on frictional slip stability of megathrust faults. Tectonophysics 600, 75–90.

Den Hartog, S.A.M., Peach, C.J., de Winter, D.A.M., Spiers, C.J., Shimamoto, T., 2012a. Frictional properties of megathrust fault gouges at low sliding velocities: new data on effects of normal stress and temperature. J. Struct. Geol. 38 (SI), 156–171.

Den Hartog, S.A.M., Niemeijer, A.R., Spiers, C.J., 2012b. New constraints on megathrust slip stability under subduction zone P–T conditions. Earth Planet. Sci. Lett. 353–354, 240–252.

Den Hartog, S.A.M., Niemeijer, A.R., Spiers, C.J., 2013. Friction on subduction megathrust faults: beyond the illite-muscovite transition. Earth Planet. Sci. Lett. 373, 8–19.

Dieterich, J.H., 1979. Modeling of rock friction 1. Experimental results and constitutive equations. J. Geophys. Res. 84, 2161–2168.

Dragert, H., Wang, K., James, T.S., 2001. A silent slip event on the deeper Cascadia subduction interface. Science 292, 1525–1528.

Ernst, W.G., 1966. Synthesis and stability relations of ferrotremolite. Am. J. Sci. 264, 36–65.

Fagereng, Å., 2011. Geology of the seismogenic subduction thrust interface. In: Fagereng, Å., Toy, V.G., Rowland, J.V. (Eds.), Geology of the Earthquake Source: A Volume in Honour of Rick Sibson. 359. Geological Society, London, Special Publications, pp. 55–76.

Fagereng, Å., Sibson, R.H., 2010. Mélange rheology and seismic style. Geology 38, 751–754.

Faulkner, D.R., Sánchez-Roa, C., Boulton, C., Den Hartog, S.A.M., 2018. Pore fluid pressure development in compacting fault gouge in theory, experiments, and nature. J. Geophys. Res. 123, 226–241.

Frost, B.R., Frost, C.D., 2013. Essentials of Igneous and Metamorphic Petrology. Cambridge University Press, Cambridge (303 pp.).

Hacker, B.R., Abers, G.A., Peacock, S.M., 2003. Subduction factory 1. Theoretical mineralogy, densities, seismic wave speeds, and H_2O contents. J. Geophys. Res. 108. https://doi.org/10.1029/2001JB001127.

He, C., Wong, T., Beeler, N.M., 2003. Scaling of stress drop with recurrence interval and loading velocity for laboratory derived fault strength relations. J. Geophys. Res. 108, 2037. https://doi.org/10.1029/2002JB001890.

He, C., Wang, Z., Yao, W., 2007. Frictional sliding of gabbro gouge under hydrothermal conditions. Tectonophysics 445, 353–362.

Hellebrekers, N., Niemeijer, A.R., Fagereng, Å., Manda, B., Mvula, R.L.S., 2019. Lower crustal earthquakes in the East African Rift System: insights from frictional properties of rock samples from the Malawi rift. Tectonophysics 767, 228167. https://doi.org/10.1016/j.tecto.2019.228167.

Heuret, A., Conrad, C.P., Funiciello, F., Lallemand, S., Sandri, L., 2012. Relation between subduction megathrust earthquakes, trench sediment thickness and upper plate strain. Geophys. Res. Lett. 39, L05304. https://doi.org/10.1029/2011GL050712.

Hirauchi, K., Katayama, I., Uehara, S., Miyahara, M., Takai, Y., 2010. Inhibition of subduction thrust earthquakes by low-temperature plastic flow in serpentine. Earth Planet. Sci. Lett. 295, 349–357.

Hyndman, R.D., Yamano, M., Oleskevich, D.A., 1997. The seismogenic zone of subduction thrust faults. Island Arc 6, 244–260.

Ikari, M.J., Saffer, D.M., Marone, C., 2009. Frictional and hydrologic properties of clay-rich fault gouge. J. Geophys. Res. 114. https://doi.org/10.1029/2008JB006089.

Ikari, M.J., Niemeijer, A.R., Spiers, C.J., Kopf, A., Saffer, D.M., 2013. Experimental evidence linking slip stability with seafloor lithology and topography at the Costa Rica convergent margin. Geology 41, 891–894.

Imon, R., Okudaira, T., Kanagawa, K., 2004. Development of shape- and lattice preferred orientations of amphibole grains during initial cataclastic deformation and subsequent deformation by dissolution-precipitation creep in amphibolites from the Ryoke metamorphic belt, SW Japan. J. Struct. Geol. 26, 793–805.

Jenkins, D.M., Bozhilov, K.N., 2003. Stability and thermodynamic properties of ferro-actinolite: a re-investigation. Am. J. Sci. 303, 723–752.

Kodaira, S., Iidaka, T., Kato, A., Park, J.-O., Iwasaki, T., Kaneda, Y., 2004. High pore fluid pressure may cause silent slip in the Nankai Trough. Science 304, 1295–1298.

Kurzawski, R.M., Niemeijer, A.R., Stipp, M., Charpentier, D., Behrmann, J.H., Spiers, C.J., 2018. Frictional properties of subduction input sediments at an erosive convergent continental margin and related controls on décollement slip modes: the Costa Rica seismogenesis project. J. Geophys. Res. 123, 8385–8408.

Lockner, D.A., Summers, R., Byerlee, J.D., 1986. Effects of temperature and sliding rate on frictional strength of granite. Pure Appl. Geophys. 124 (3), 445–469.

Logan, J.M., Friedman, M., Higgs, N., Dengo, C.A., Shimamoto, T., 1979. Experimental studies of simulated gouge and their application to studies of natural fault zones. In: Speed, R., Sharp, R. (Eds.), Proceedings of Conference VIII—Analysis of Actual Fault Zones in Bedrock. USGS, Menlo Park, pp. 305–343.

Marone, C., 1998a. Laboratory-derived friction laws and their application to seismic faulting. Annu. Rev. Earth Planet. Sci. 26, 643–696.

Marone, C., 1998b. The effect of loading rate on static friction and the rate of fault healing

during the earthquake cycle. Nature 391, 69–72.
Marone, C., Vidale, J.E., Ellsworth, W., 1995. Fault healing inferred from time dependent variations in source properties of repeating earthquakes. Geophys. Res. Lett. 22, 3095–3098.
Moore, D.E., Lockner, D.A., 2013. Chemical controls on fault behaviour: weakening of serpentinite sheared against quartz-bearing rocks and its significance for fault creep in the San Andreas system. J. Geophys. Res. 118. https://doi.org/10.1002/jgrb.50140.
Niemeijer, A.R., 2018. Velocity-dependent slip weakening by the combined operation of pressure solution and foliation development. Sci. Rep. 8. https://doi.org/10.1038/s41598-018-22889-3.
Niemeijer, A.R., Spiers, C.J., 2006. Velocity dependence of strength and healing behaviour in simulated phyllosilicate-bearing fault gouge. Tectonophysics 427, 231–253.
Niemeijer, A.R., Vissers, R.L.M., 2014. Earthquake rupture propagation inferred from the spatial distribution of fault rock frictional properties. Earth Planet. Sci. Lett. 396, 154–164.
Niemeijer, A.R., Boulton, C., Toy, V.G., Townend, J., Sutherland, R., 2016. Large-displacement, hydrothermal properties of DFDP-1 fault rocks, Alpine Fault, New Zeland: implications for deep rupture propagation. J. Geophys. Res. 121, 624–647.
Nishiyama, T., 1989. Petrological study of the Nagasaki metamorphic rocks in the Nishisonogi Peninsula – with special reference to the greenrock complex and the reaction-enhanced ductility. Mem. Geol. Soc. Jpn. 33, 237–257 (Japanese with English abstract).
Obara, K., 2002. Non-volcanic deep tremor associated with subduction in southwest Japan. Science 296, 1679–1681. https://doi.org/10.1126/science.1070378.
Obara, K., Kato, A., 2016. Connecting slow earthquakes to huge earthquakes. Science 353, 253–257.
Okamoto, A.S., Verberne, B.A., Niemeijer, A.R., Takahashi, M., Shimizu, I., Ueda, T., Spiers, C.J., 2019. Frictional properties of simulated chlorite gouge at hydrothermal conditions: implications for subduction megathrusts. J. Geophys. Res. 124, 4545–4565.
Okazaki, K., Hirth, G., 2016. Dehydration of lawsonite could directly trigger earthquakes in subducting oceanic crust. Nature 530, 81–84.
Peacock, S.M., Christensen, N.I., Bostock, M.G., Audet, P., 2011. High pore pressures and porosity at 35 km depth in the Cascadia subduction zone. Geology 39, 471–474.
Peng, Z., Gomberg, J., 2010. An integrated perspective of the continuum between earthquakes and slow-slip phenomena. Nat. Geosci. 3, 599–607.
Rabinowitz, H.S., Savage, H.M., Skarbek, R.M., Ikari, M.J., Carpenter, B.M., Collettini, C., 2018. Frictional behavior of input sediments to the Hikurangi Trench, New Zealand. Geochem. Geophys. Geosyst. 19, 2973–2990.
Raymond, L.A., 2019. Perspectives on the roles of melanges in subduction accretionary complexes: a review. Gondwana Res. 74, 68–89.
Reinen, L.A., Weeks, J.D., 1993. Determination of rock friction constitutive parameters using an iterative least squares inversion method. J. Geophys. Res. 98 (B9), 15937–15950.
Rice, J.R., Ruina, A., 1983. Stability of steady frictional slipping. J. Appl. Mech. 50, 343–349.
Ruina, A., 1983. Slip instability and state variable friction laws. J. Geophys. Res. 88, 10359–10370.
Sakakibara, M., Ota, T., 1994. Metamorphic evolution of the Kamuikotan high-pressure and low-temperature metamorphic rocks in central Hokkaido, Japan. J. Geophys. Res. 99, 22221–22235.
Sawai, M., Hirose, T., Kameda, J., 2014. Frictional properties of incoming pelagic sediments at the Japan Trench: implications for large slip at a shallow plate boundary during the 2011 Tohoku earthquake. Earth Planets Space 66, 65. https://doi.org/10.1186/18805981-66-65.
Sawai, M., Niemeijer, A.R., Plümper, O., Hirose, T., Spiers, C.J., 2016. Nucleation of frictional instability caused by fluid pressurization in subducted blueschist. Geophys. Res. Lett. 43, 2543–2551.
Sawai, M., Niemeijer, A.R., Hirose, T., Spiers, C.J., 2017. Frictional properties of JFAST core samples and implications for slow earthquakes at the Tohoku subduction zone. Geophys. Res. Lett. 44, 8822–8831.
Scholz, C.H., 1998. Earthquakes and friction laws. Nature 391, 37–42.
Segall, P., Rice, J.R., 2006. Does shear heating of pore fluid contribute to earthquake nucleation? Journal of Geophysical Research 111 (B09316), 1–17. https://doi.org/10.1029/2005JB004129. B09316.
Shelly, D.R., Beroza, G.C., Ide, S., Nakamura, S., 2006. Low-frequency earthquakes in Shikoku, Japan, and their relation to episodic tremor and slip. Nature 442, 188–191.
Simons, M., Minson, S.E., Sladen, A., Ortega, F., Jiang, J., Owen, S.E., Meng, L., Ampuero, J.-P., Wei, S., Chu, R., Helmberger, D.V., Kanamori, H., Hetland, E., Moore, A.W., Webb, F.H., 2011. The 2011 magnitude 9.0 Tohoku-Oki Earthquake: mosaicking the megathrust from seconds to centuries. Science 332, 1421–1426.
Sorensen, S.S., Sisson, V.B., Harlow, G.E., Avé Lallemant, H.G., 2010. Element residence and transport during subduction-zone metasomatism: evidence from a jadeitite-serpentinite contact, Guatemala. Int. Geol. Rev. 52, 899–940.
Spudich, P., Orcutt, J., 1980. A new look at the seismic velocity structure of the oceanic crust. Rev. Geophys. Space Ge. 18, 627–645.
Takahashi, M., Mizoguchi, K., Kitamura, K., Masuda, K., 2007. Effects of clay content on the frictional strength and fluid transport property of faults. J. Geophys. Res. 112, B08206. https://doi.org/10.1029/2006JB004678.
Takahashi, M., Uehara, S.-I., Mizoguchi, K., Shimizu, I., Okazaki, K., Masuda, K., 2011. On the transient response of serpentine (antigorite) gouge to stepwise changes in slip velocity under high-temperature conditions. J. Geophys. Res. 116. https://doi.org/10.1029/2010JB008062.
Takeshita, T., Yagi, K., Gouzu, C., Hironobu, H., Itaya, T., 2015. Extensive normal faulting during exhumation revealed by the spatial variation of phengite K-Ar ages in the Sambagawa metamorphic rocks, central Shikoku, SW Japan. Island Arc 24, 245–262.
Tarling, M.S., Smith, S.A.F., Scott, J.M., 2019. Fluid overpressure from chemical reactions in serpentinite within the source region of deep episodic tremor. Nat. Geosci. 12, 1034–1042.
Tenthorey, E., Cox, S.F., 2006. Cohesive strengthening of fault zones during the interseismic period: an experimental study. J. Geophys. Res. 111, B09202. https://doi.org/10.1029/2005JB004122.
Uchida, N., Iinuma, T., Nadeau, R.M., Bürgmann, R., Hino, R., 2016. Periodic slow slip triggers megathrust earthquakes in northeastern Japan. Science 351, 488–492.
Ujiie, K., Saishu, H., Fagereng, Å., Nishiyama, N., Otsubo, M., Masuyama, H., Kagi, H., 2018. An explanation of episodic tremor and slow slip constrained by crack-seal veins and viscous shear in subduction mélange. Geophys. Res. Lett. 45, 5371–5379.
Verberne, B.A., He, C., Spiers, C.J., 2010. Frictional properties of sedimentary rocks and natural fault gouge from the Longmenshan Fault Zone, Sichuan, China. Bull. Seismol. Soc. Am. 100, 2767–2790.
Verberne, B.A., de Bresser, J.H.P., Niemeijer, A.R., Spiers, C.J., de Winter, D.A.M., Plümper, O., 2013. Nanocrystalline slip zones in calcite fault gouge show intense crystallographic preferred orientation: crystal plasticity at sub-seismic slip rates at 18–150°C. Geology 41, 863–866.
Verberne, B.A., Niemeijer, A.R., De Bresser, J.H.P., Spiers, C.J., 2015. Mechanical behavior and microstructure of simulated calcite fault gouge sheared at 20–600°C: implications for natural faults in limestones. J. Geophys. Res. 120, 8169–8196.
Winter, J.D., 2001. An Introduction to Igneous and Metamorphic Petrology. Prentice Hall, Upper Saddle River, New Jersey, pp. 697.
Wonnacott, T.H., Wonnacott, R.J., 1990. Introductory Statistics. John Wiley & Sons, Inc., New York, pp. 710.
Yasuhara, H., Marone, C., Elsworth, D., 2005. Fault zone re-strengthening and frictional healing: the role of pressure solution. J. Geophys. Res. 110, B06310. https://doi.org/10.1029/2004JB003327.
Yoshioka, S., Suminokura, Y., Matsumoto, T., Nakajima, J., 2013. Two-dimensional thermal modelling of subduction of the Philippine Sea plate beneath southwest Japan. Tectonophysics 608, 1094–1108.
Zhang, L., He, C., 2016. Frictional properties of phyllosilicate-rich mylonite and conditions for the brittle-ductile transition. J. Geophys. Res. 121, 3017–3047.
Zhang, L., He, C., Liu, Y., Lin, J., 2017. Frictional properties of the South China Sea oceanic basalt and implications for strength of the Manila subduction zone. Mar. Geol. 394, 16–29.